AIMS Mathematics

https://www.aimspress.com/journal/Math

AIMS Mathematics, 11(3): 5492–5531.
DOI:10.3934/math.2026227
Received: 23 October 2025
Revised: 03 February 2026
Accepted: 06 February 2026
Published: 4 March 2026

Research article

Data-driven variable-order fractional control for grid resilience: A hybrid Caputo-Hadamard framework validated with US power system data

Kinda Abuasbeh[1] **and Meraa Arab**[2,*]

[1] Department of Robotics and Control Engineering, College of Engineering, Al Zaytoonah University of Science and Technology, Salfit, P390, Palestine

[2] Department of Mathematics, College of Science, King Faisal University, P.O. Box 400, Al-Ahsa, 31982, Saudi Arabia

* **Correspondence:** Email: marab@kfu.edu.sa.

Abstract: The rapid integration of inverter-based renewable resources poses significant challenges to power systems' stability and resilience. This paper presents a data-driven variable-order fractional control framework that enhances grids' resilience through adaptive memory management. The proposed controller employs a hybrid Caputo-Hadamard structure, in which the fractional order $\alpha(t)$ adapts in real time according to wide-area frequency measurements. The Caputo component captures short-memory transient dynamics associated with power electronic responses, while the Hadamard component represents long-memory logarithmic effects arising from variability in the load and renewable generation. Rigorous stability analysis establishes Mittag-Leffler stability under bounded order variation and Ulam-Hyers practical stability, ensuring robustness against modeling uncertainties and numerical discretization errors. Numerical validation using realistic US power system data from Pennsylvania-New Jersey-Maryland (PJM) Interconnection, California Independent System Operator (CAISO), National Renewable Energy Laboratory (NREL), and Frequency Monitoring Network (FNET/GridEye) demonstrates consistently improved performance compared with integer-order and fixed-order fractional controllers, including up to 67% reduction in voltage overshoot and 72% reduction in the duration of rate of change of frequency violations under compound disturbance scenarios. The proposed framework provides a mathematically rigorous and practically viable approach for adaptive control in renewable-rich power systems, aligning with ongoing grid modernization efforts that seek to balance fast transient response with long-term stability in the system.

Keywords: fractional-order control; variable-order systems; power grid resilience; data-driven control; adaptive control
Mathematics Subject Classification: 26A33, 68T09, 93A16, 93B35, 93C10, 93C40, 93C95, 93D23

1. Introduction

The rapid transformation of the US electric power system, driven by the accelerating deployment of inverter-based resources (IBRs) such as solar, wind, and battery storage, presents a critical challenge to the grids' stability and control. This transition, while essential for decarbonization, reduces systems' inertia and introduces fast, complex dynamics that traditional synchronous-machine-era paradigms are ill-equipped to handle [1]. Recognizing this, the US Department of Energy's (DoE'S) Grid Modernization Initiative (GMI) has explicitly prioritized the development of advanced control frameworks to ensure resilience, reliability, and security [2]. This urgency is echoed by reliability authorities like the North American Electric Reliability Corporation (NERC), which has documented emerging stability risks and the need for robust mitigation strategies tailored to IBR-dominated grids [3].

In parallel, the proliferation of wide-area monitoring systems (WAMS) like the Frequency Monitoring Network (FNET/GridEye) network provides an unprecedented, real-time view of grid dynamics through global positioning system (GPS)-synchronized measurements of frequency, phase angle, and rate of change of frequency (RoCoF) across the continent [4]. This rich data source, combined with open-access US datasets from the National Renewable Energy Laboratory (NREL WIND Toolkit [5], National Solar Radiation Database (NSRDB) [6]), and system operators (PJM Interconnection [7], California Independent System Operator (CAISO) [8]), creates a unique opportunity to ground control design in empirically validated, realistic scenarios that reflect the true variability and disturbance profiles of the modern US grid.

Within this context, fractional-order calculus has emerged as a powerful mathematical framework for modeling the hereditary and memory-laden phenomena inherent in complex power systems [9]. Fractional-order proportional integral derivative (FOPID) controllers, in particular, have demonstrated superior performance over their integer-order counterparts by providing additional tuning flexibility for managing non-linearities and long-range dependencies [10]. However, a significant limitation persists in the state-of-the-art: The reliance on fixed-order fractional operators. This approach fails to capture the time-varying, multi-scale nature of grid dynamics, where the memory required to damp a fast RoCoF event differs fundamentally from that needed to manage slow, logarithmic load and renewable fluctuations. Recent works in adaptive control have shown promising results in handling such complexities. For instance, adaptive finite-time consensus protocols for high-order nonlinear multi-agent systems [11] and robust sliding mode control for discrete fractional chaotic systems [12] highlight the effectiveness of adaptive mechanisms in improving convergence and resource efficiency. Similarly, hybrid adaptive strategies for fractional-order neural networks [13–15] and reaction-diffusion systems [16, 17] demonstrate the potential of combining fractional operators with real-time adaptation to achieve enhanced stability and synchronization under delays and uncertainties.

While recent works have explored adaptive fractional control [18] and data-driven methods for power systems [19], a synthesis that dynamically couples the controller's fundamental structure to real-time, wide-area grid measurements remains an open and compelling research frontier. The integration of variable-order fractional calculus with data-driven adaptation offers a promising pathway. This integration is evidenced by studies on fractional-order delayed biological systems [20] and boundary value problems with mixed perturbations [21]. These works underscore the importance of adaptive fractional frameworks in capturing multi-scale dynamics and ensuring solvability and stability under disturbances. Furthermore, advanced control techniques such as finite-time adaptive sliding mode control for uncertain chaotic systems [22] and global Mittag-Leffler synchronization of coupled fractional reaction-diffusion networks [23] provide robust solutions for managing uncertainties and external disturbances in complex nonlinear systems, which are critical challenges in renewable-rich power grids.

The novelty and originality of this work lie in its integrated, data-driven approach to bridging this gap. We propose a hybrid variable-order fractional control framework where the differential order $\alpha(t) \in (0, 1)$ is dynamically adapted based on real-time frequency deviation and RoCoF measurements from the US FNET/GridEye system. This creates an adaptive "grid memory" that instinctively responds to the severity of frequency events. Furthermore, we introduce a hybrid Caputo-Hadamard formulation, uniquely employing the Caputo derivative to model short-memory transients in power-electronic responses and the Hadamard derivative to capture the long-memory, logarithmic behavior of load and renewable profiles. This hybrid model is governed by a robust control law that synergistically combines a FOPID with sliding mode control and H_∞ optimization [24], ensuring the rejection of disturbance under realistic ramp events and measurement noise derived from the NREL and Independent System Operator (ISO) datasets. The theoretical foundation is solidified by establishing the non-local Mittag-Leffler stability [25] and Ulam-Hyers practical stability [26] for the hybrid system, guaranteeing robust performance under numerical approximation and data noise—a critical consideration for practical implementation.

To provide credible and reproducible validation aligned with US national priorities, the proposed controller is rigorously tested across multiple US-centric case studies utilizing PJM Interconnection and California Independent System Operator (CAISO) operational data, NREL renewable profiles, and Frequency Monitoring Network disturbance records. By anchoring the entire research lifecycle—from design inspiration to performance validation—in authoritative US data and the strategic goals of the DoE's GMI, this work provides a direct, empirically-validated pathway for enhancing national grid resilience, renewable integration, and long-term energy security.

The remainder of the paper is structured as follows. Section 2 describes the data sources and system configuration used for validation. Section 3 introduces the hybrid Caputo-Hadamard memory functional framework. Section 4 presents the stability analysis of the control system. Section 5 provides a numerical validation and the simulation results. Finally, Section 6 concludes the paper and outlines future research directions.

2. Data sources and system description

This section details the US datasets and the microgrid configuration used to develop and validate the proposed control framework. The objective is to ground the analysis in realistic operating conditions reflective of the modern US power grid, utilizing publicly available data from national laboratories and system operators [2].

2.1. Renewable generation data

Wind power profiles were generated using data from the NREL WIND Toolkit [5]. The dataset provides high-resolution meteorological variables such as wind speed $v(t)$, air density $\rho(t)$, and temperature, from which the turbine's power output is computed using

$$P_{\mathrm{w}}(t) = \frac{1}{2}\rho(t) A C_p(t) v^3(t), \tag{2.1}$$

where A is the rotor's swept area and $C_p(t)$ is the power coefficient. Specific site locations within the PJM Interconnection and California Independent System Operator (CAISO) footprints are selected to capture regional wind characteristics across the continental United States.

Solar generation time series were derived from the NREL National Solar Radiation Database National Solar Radiation Database (NSRDB) [6], which supplies global horizontal irradiance (GHI), direct normal irradiance (DNI), and ambient temperature at a half-hourly or hourly resolution. The alternative current (AC) power from the photovoltaic (PV) array is modeled as

$$P_{\mathrm{s}}(t) = \eta A_{\mathrm{pv}}\, GHI(t)\, [1 - \beta(T_c(t) - 25)], \tag{2.2}$$

where η is panel's efficiency, β is the temperature coefficient, and $T_c(t)$ is the cell's temperature. These renewable inputs feed the generation side of the microgrid model.

2.2. Load and system operation data

Real-world load profiles were obtained from the PJM Interconnection [7] and (CAISO) [8]. PJM's data miner provides hourly metered load and generation by fuel type, while CAISO's OASIS platform supplies demand and renewable dispatch data at 5-minute resolution. The active power demand used in the simulation is expressed as follows:

$$L(t) = L_{\mathrm{base}} P_{\mathrm{pu}}(t), \qquad P_{\mathrm{pu}}(t) = \frac{P(t) - P_{\min}}{P_{\max} - P_{\min}}, \tag{2.3}$$

where L_{base} is the nominal load. Periods of high volatility and steep ramping are chosen to stress-test the controller under a realistic operating stress.

2.3. Wide-area frequency measurements

Wide-area system frequency, deviation, and (RoCoF) were obtained from the FNET/GridEye network [4]. Each frequency disturbance recorder (FDR) provides GPS-synchronized measurements of $f(t)$, from which we obtain

$$\Delta f(t) = f(t) - f_0, \qquad \mathrm{RoCoF}(t) = \frac{df(t)}{dt}, \tag{2.4}$$

where $f_0 = 60$ Hz denotes the nominal frequency. These quantities serve as direct indicators of stress in the system and are the inputs for the adaptive fractional-order law governing the variable order $\alpha(t)$:

$$\alpha(t) = \alpha_0 + \kappa_1 |\Delta f(t)| + \kappa_2 |\mathrm{RoCoF}(t)|, \tag{2.5}$$

A low-pass Savitzky-Golay filter is applied to remove high-frequency noise while preserving the dynamic content.

2.4. *Microgrid test system*

A representative hybrid microgrid is considered to evaluate the proposed control framework. The system consists of a wind turbine generator, a PV array, a battery energy storage system, and a time-varying load. All generation and storage units are interfaced through grid-forming voltage-source converters (VSCs). Unlike grid-following converters, grid-forming converters actively establish voltage and frequency references, enabling stable operation in low-inertia and islanded microgrid conditions.

2.4.1. State-space representation

Under standard averaging assumptions and small-signal modeling, the microgrid's dynamics can be written in a compact state-space form as follows:

$$\dot{\mathbf{x}}(t) = \mathbf{A}\mathbf{x}(t) + \mathbf{B}\mathbf{u}(t) + \mathbf{D}\mathbf{d}(t), \tag{2.6}$$

where $\mathbf{x}(t) \in \mathbb{R}^n$ denotes the state vector (including the frequency deviation, voltage deviation, and the converter's internal states), $\mathbf{u}(t)$ represents the control input generated by the grid-forming controllers, and $\mathbf{d}(t)$ captures exogenous disturbances arising from renewable fluctuations and load variations. The matrices $\mathbf{A}$, $\mathbf{B}$, and $\mathbf{F}$ are constant system matrices with compatible dimensions determined by the microgrid's configuration.

2.4.2. Hybrid fractional-order reformulation

To capture the memory and hereditary effects that are not adequately represented by the integer-order model, the classical time derivative in (2.6) is replaced by a variable-order hybrid fractional operator. The resulting fractional-order state-space model is expressed as follows:

$$\mathcal{M}^{\alpha(t)}[\mathbf{x}](t) = \mathbf{A}\mathbf{x}(t) + \mathbf{B}\mathbf{u}(t) + \mathbf{F}\mathbf{d}(t), \tag{2.7}$$

where $\mathcal{M}^{\alpha(t)}$ denotes the hybrid Caputo–Hadamard fractional derivative operator of time-varying order $\alpha(t) \in (0, 1)$.

The hybrid operator is defined as

$$\mathcal{M}^{\alpha(t)}[\mathbf{x}](t) = \lambda\, {}^{C}D^{\alpha(t)}\mathbf{x}(t) + (1 - \lambda)\, {}^{H}D^{\alpha(t)}\mathbf{x}(t), \tag{2.8}$$

where ${}^{C}D^{\alpha(t)}(\cdot)$ and ${}^{H}D^{\alpha(t)}(\cdot)$ denote the variable-order Caputo and Hadamard fractional derivatives, respectively, and $\lambda \in [0, 1]$ is a weighting parameter that balances short-memory and long-memory effects.

The matrix $\mathbf{A}$ in (2.7) represents the system dynamics matrix and should not be confused with the rotor's swept area A appearing in the wind turbine power model in Section 2.1. The distinction is maintained throughout the paper by using boldface notation for matrices.

2.5. *Data preprocessing and integration*

All external data streams are synchronized to coordinated universal time (UTC) and resampled to a uniform 1-s time step for dynamic simulation. Short data gaps (less than 30 minutes) are interpolated linearly. Renewable generation and load profiles are normalized to the microgrid's base power S_{base}. The unified dataset is defined as

$$\mathcal{D} = \{P_{\text{w}}(t), P_{\text{s}}(t), L(t), \Delta f(t), \text{RoCoF}(t)\},$$

which drives both the simulation model and the adaptive controller. All processing steps follow reproducible scripts and adhere to the original data licenses.

This section has described the US datasets and system model forming the foundation for the proposed hybrid fractional-order control framework. The following section formulates the hybrid Caputo-Hadamard model and the design of the adaptive controller.

3. Hybrid memory functional framework

3.1. Motivation: Multi-scale memory in power grids

Modern power grids with high penetration of inverter-based resources exhibit dynamics across multiple time scales. Fast transients such as converter switching and RoCoF events require short-memory responses for rapid damping. In contrast, slow variations including load patterns and renewable power ramps benefit from long-memory smoothing. Traditional fractional operators with single memory kernels, whether power-law or logarithmic, cannot simultaneously capture both regimes effectively. This fundamental limitation motivates the design of a structured memory functional that combines complementary memory characteristics appropriate for modern grid applications.

3.2. Definitions and mathematical foundation

Definition 3.1. *(Function spaces) Let* $[0, T]$ *denote the operating horizon. We consider signals in the intersection space*

$$\mathcal{X} = W^{1,2}[0, T] \cap \left\{ x : \int_0^T |x(\tau)|^2 \frac{d\tau}{\tau} < \infty \right\}$$

equipped with the norm $\|x\|_{\mathcal{X}} = \|x\|_{W^{1,2}} + \|x\|_{L^2(d\tau/\tau)}$.

Definition 3.2. *(Individual memory contributions) For a signal* $x \in \mathcal{X}$ *and a time-varying fractional order* $\alpha(t) \in C^1[0, T]$ *satisfying* $0 < \alpha_{\min} \leq \alpha(t) \leq \alpha_{\max} < 1$*, we define two memory contributions.*

The Caputo-type memory contribution is

$$C^{\alpha(t)}[x](t) = \frac{1}{\Gamma(1 - \alpha(t))} \int_0^t (t - \tau)^{-\alpha(t)} \dot{x}(\tau)\, d\tau.$$

The Hadamard-type memory contribution is

$$\mathcal{H}^{\alpha(t)}[x](t) = \frac{1}{\Gamma(1 - \alpha(t))} \int_{0+}^t \left(\log \frac{t}{\tau}\right)^{-\alpha(t)} \frac{d}{d\tau}(\tau x(\tau)) \frac{d\tau}{\tau}.$$

The function $\Gamma(\cdot)$ *denotes the Gamma function [9].*

Definition 3.3. *(Hybrid memory functional) For a weighting parameter* $\lambda \in [0, 1]$*, the hybrid caputo-hadamard memory functional (HCMF) is defined as*

$$\mathcal{M}^{\alpha(t)}[x](t) = \lambda\, C^{\alpha(t)}[x](t) + (1 - \lambda)\, \mathcal{H}^{\alpha(t)}[x](t).$$

3.3. Key properties and well-posedness

The following theorem establishes the fundamental properties of the proposed hybrid memory functional.

Theorem 3.1. *(Well-posedness of the HCMF) For any $x \in \mathcal{X}$ and $\alpha(t)$ satisfying $|\dot{\alpha}(t)| \leq \rho$, the hybrid memory functional $\mathcal{M}^{\alpha(t)}[x](t)$ satisfies the following properties.*

(1) Existence. The functional $\mathcal{M}^{\alpha(t)}[x](t)$ exists for all $t \in [0, T]$.

(2) Boundedness. A constant $C = C(\lambda, \alpha_{\max}, \rho) > 0$ exists such that

$$\|\mathcal{M}^{\alpha(t)}[x]\|_{L^2} \leq C\|x\|_{\mathcal{X}} \quad \textit{uniformly in } t \in [0, T].$$

(3) Linearity. For any scalars $a, b \in \mathbb{R}$ and signals $x_1, x_2 \in \mathcal{X}$, we have

$$\mathcal{M}^{\alpha(t)}[ax_1 + bx_2] = a\mathcal{M}^{\alpha(t)}[x_1] + b\mathcal{M}^{\alpha(t)}[x_2].$$

Proof sketch. The existence follows from the absolute integrability of the kernels $(t - \tau)^{-\alpha(t)}$ and $(\log t/\tau)^{-\alpha(t)}$ over $[0, T]$. The boundedness uses Young's convolution inequality adapted for time-varying kernels, under the boundedness of $\alpha(t)$ and its derivative $\dot{\alpha}(t)$, similar to the techniques in [27]. The linearity is immediate from the linearity of the integral operators. The complete proof is provided in Appendix A. □

Lemma 3.1. *(Physical interpretation) The two components of the HCMF correspond to distinct physical phenomena in power grids. The Caputo-type contribution $\mathcal{C}^{\alpha(t)}$ models fast, exponentially decaying transients typical of power electronic responses. The Hadamard-type contribution $\mathcal{H}^{\alpha(t)}$ captures slow, logarithmic variations observed in the load and renewable generation profiles. The weighting parameter λ balances the relative emphasis between these fast and slow dynamic regimes.*

Remark 3.1. *(Conceptual positioning) It is essential to clarify that $\mathcal{M}^{\alpha(t)}$ is not introduced as a novel fractional derivative operator in the pure mathematical sense. Instead, it is a control-theoretic construct—a structured memory functional designed to capture multi-scale dynamic effects observed in power systems. Mathematically, it operates as a well-defined linear functional on $\mathcal{X}$ as established in Theorem 3.1. Physically, it provides a parsimonious representation of multi time-scale memory effects in inverter-based grids. This distinction preserves mathematical rigor while enabling practical innovation in control design.*

3.4. State-space representation with the HCMF

The microgrid's dynamics are formulated within the HCMF framework via the following variable-order fractional memory-based state-space representation:

$$\mathcal{M}^{\alpha(t)}[\mathbf{x}](t) = \mathbf{A}\mathbf{x}(t) + \mathbf{B}\mathbf{u}(t) + \mathbf{F}\mathbf{d}(t), \tag{3.1}$$

where $\mathbf{x}(t) \in \mathbb{R}^n$ denotes the state vector. For the considered microgrid configuration, this vector comprises the direct-axis current $i_d(t)$, the quadrature-axis current $i_q(t)$, the direct current (DC)-link voltage $v_{\text{dc}}(t)$, and the system's frequency deviation $\Delta\omega(t)$. Thus

$$\mathbf{x}(t) = \begin{bmatrix} i_d(t) & i_q(t) & v_{\mathrm{dc}}(t) & \Delta\omega(t) \end{bmatrix}^\top .$$

The control input vector $\mathbf{u}(t) \in \mathbb{R}^m$ acts on the grid-forming voltage-source converters, while $\mathbf{d}(t) \in \mathbb{R}^p$ aggregates the external disturbances arising from renewable generation fluctuations and load variations. The matrices $\mathbf{A} \in \mathbb{R}^{n\times n}$, $\mathbf{B} \in \mathbb{R}^{n\times m}$, and $\mathbf{F} \in \mathbb{R}^{n\times p}$ characterize the system's dynamics, input coupling, and disturbance channels, respectively. Their numerical values, derived from typical community-scale microgrid parameters, are provided in Section 5.

The time-varying fractional order $\alpha(t)$ adapts in real time according to the wide-area frequency measurements according to the affine adaptation law

$$\alpha(t) = \alpha_0 + \kappa_1|\Delta f(t)| + \kappa_2|\mathrm{RoCoF}(t)|, \tag{3.2}$$

where $\Delta f(t) = \Delta\omega(t)/(2\pi)$ represents the system's frequency deviation from the nominal value (60 Hz) and $\mathrm{RoCoF}(t)$ denotes its rate of change. The constants $\kappa_1, \kappa_2 > 0$ are calibration gains determined from historical FNET/GridEye data. To ensure mathematical well-posedness and physical realizability, the adapted order is constrained to the interval

$$0.1 \leq \alpha(t) \leq 0.9 \quad \text{for all } t \geq 0.$$

This saturation prevents singular behavior at the boundaries $\alpha = 0$ and $\alpha = 1$, while maintaining the fractional character of the dynamics.

The control objective is to design $\mathbf{u}(t)$ such that the system (3.1) achieves frequency regulation and voltage stability despite the disturbances $\mathbf{d}(t)$, with the adaptive order $\alpha(t)$ providing a tunable memory mechanism within the bounds established in Section 3.3, responding to grid stress levels indicated by $|\Delta f|$ and $|\mathrm{RoCoF}|$.

3.5. *Selection of the hybrid weight λ*

The hybrid weighting parameter $\lambda \in [0, 1]$ determines the relative emphasis between the Caputo-type short-memory component and the Hadamard-type long-memory component within the HCMF. Empirical analysis of operational data from US power grids, combined with representative numerical simulations across various disturbance scenarios, yields the following guidelines for selecting λ.

For grid conditions dominated by fast transients, such as converter switching events and rapid RoCoF variations, a higher value of $\lambda \approx 0.8$ appropriately emphasizes the Caputo component to ensure effective damping of short-term oscillations. Conversely, for scenarios characterized by slow variations in load demand and renewable generation, a lower value $\lambda \approx 0.4$ gives greater weight to the Hadamard component, promoting smooth tracking of long-term trends.

In the mixed operational environments typical of modern microgrids with both inverter-based resources and conventional loads, a balanced intermediate value provides optimal performance. Based on comprehensive simulation studies presented in Section 5, the value $\lambda = 0.7$ achieves an effective compromise between transient response speed and steady-state accuracy while remaining consistent with the stability conditions derived in Section 4. This selection ensures that the controller responds promptly to fast disturbances while maintaining smooth recovery during slow variations.

It is important to note that while λ is treated as a fixed parameter in this study for clarity of analysis, the framework naturally accommodates a time-varying $\lambda(t)$ should future applications require adaptive balancing of the memory components. The sensitivity of control performance to variations in λ is examined quantitatively in Section 5.4 (Parametric Sensitivity and Visualization).

The constants $\kappa_1, \kappa_2 > 0$ are calibration gains determined from historical FNET/GridEye data. To ensure mathematical well-posedness and physical realizability, the adapted order is constrained to the interval

$$0.1 \leq \alpha(t) \leq 0.9 \quad \text{for all } t \geq 0.$$

This saturation prevents singular behavior at the boundaries $\alpha = 0$ and $\alpha = 1$, while maintaining the fractional character of the dynamics.

3.6. Controller design with the HCMF

The control law employs the HCMF within a composite structure that combines FOPID action with sliding mode compensation for enhanced robustness. The total control input is given by

$$\mathbf{u}(t) = \mathbf{u}_{\text{FOPID}}(t) + \mathbf{u}_{\text{SMC}}(t), \tag{3.3}$$

where $\mathbf{u}_{\text{FOPID}}(t)$ represents the FOPID component and $\mathbf{u}_{\text{SMC}}(t)$ denotes the sliding mode compensation term.

The FOPID component is formulated as

$$\mathbf{u}_{\text{FOPID}}(t) = \mathbf{K}_p\mathbf{e}(t) + \mathbf{K}_i\mathcal{I}^{\mu(t)}[\mathbf{e}](t) + \mathbf{K}_d\mathcal{D}^{\nu(t)}[\mathbf{e}](t), \tag{3.4}$$

where $\mathcal{I}^{\mu(t)}$ denotes the variable-order Caputo fractional integral, defined as

$$\mathcal{I}^{\mu(t)}[e](t) = \frac{1}{\Gamma(\mu(t))}\int_0^t (t-\tau)^{\mu(t)-1}e(\tau)\,d\tau,$$

with $\mu(t) = \phi_1\alpha(t)$ and $\phi_1 > 0$. The derivative operator $\mathcal{D}^{\nu(t)}$ follows a similar variable-order Caputo definition.

The sliding mode component is derived from the fractional sliding surface

$$\mathbf{s}(t) = \mathbf{e}(t) + \gamma\mathcal{I}^{-\beta}[\mathbf{e}](t), \quad 0 < \beta < 1,\ \gamma > 0, \tag{3.5}$$

and takes the form

$$\mathbf{u}_{\text{SMC}}(t) = -\mathbf{K}_s\,\text{sgn}(\mathbf{s}(t)) - \mathbf{K}_r\mathbf{s}(t), \tag{3.6}$$

where $\mathbf{K}_s, \mathbf{K}_r$ are positive definite gain matrices and $\text{sgn}(\cdot)$ denotes the signum function applied element-wise.

The control gains $\mathbf{K}_p, \mathbf{K}_i, \mathbf{K}_d, \mathbf{K}_s, \mathbf{K}_r$ are optimized via H_∞ synthesis to minimize disturbance amplification while ensuring closed-loop stability. The resulting linear matrix inequality formulation and a detailed stability analysis are presented in Section 4.

3.7. Gain computation via the feasibility of the linear matrix inequality (offline)

This subsection clarifies the procedure for obtaining the controller gains $\mathbf{K}_p, \mathbf{K}_i, \mathbf{K}_d, \mathbf{K}_s, \mathbf{K}_r$ used in the control law (3.3)–(3.6). The gains are computed offline by solving the linear matrix inequality (LMI) condition presented in Theorem 4.1. This clarification is provided to explicitly connect the stability of the LMI in Section 4 with the numerical controller gains reported in Table 4.

Using the nominal system matrices $\mathbf{A}, \mathbf{B}, \mathbf{F}$ (Table 3) and the order-variation bound $\rho = 0.03\ \mathrm{s}^{-1}$ (Remark 4.1), we search for symmetric positive definite matrices $\mathbf{P}, \mathbf{Q} \in \mathbb{R}^{n\times n}$ and a scalar $\gamma > 0$ such that the LMI (4.2) is feasible. A standard change of the variables $\mathbf{Y} = \mathbf{KP}$ is employed to express the controller gains within the LMI feasibility framework, where $\mathbf{K}$ collects the controller gains consistent with the structure of (3.3)–(3.6).

The LMI feasibility problem is solved using the MATLAB LMI Toolbox (function `feasp`). From the feasible solution, the gain matrix is recovered as $\mathbf{K} = \mathbf{YP}^{-1}$. This matrix is then partitioned according to the control structure (3.3)–(3.6) to extract the individual gain matrices $\mathbf{K}_p, \mathbf{K}_i, \mathbf{K}_d, \mathbf{K}_s, \mathbf{K}_r$. The numerical values obtained for the considered microgrid configuration are listed in Table 4.

These gains remain fixed during online operation. Together with the real-time adaptation of the fractional order $\alpha(t)$ via (3.2), they ensure that the closed-loop system satisfies the stability and robustness guarantees established in Theorems 4.1 and 4.2 for all admissible values of$\alpha(t)$ satisfying Assumption 4.1.

4. Stability analysis of the HCMF-based control system

4.1. Preliminaries and assumptions

4.1.1. Closed-loop system formulation

The closed-loop dynamics under the hybrid memory functional controller developed in Section 3 are obtained by substituting the control law (3.3) into the open-loop state-space representation (2.7). This yields the compact form

$$\mathcal{M}^{\alpha(t)}[\mathbf{x}](t) = \mathbf{A}_{\mathrm{cl}}\mathbf{x}(t) + \mathbf{F}\mathbf{d}(t), \tag{4.1}$$

where $\mathbf{A}_{\mathrm{cl}} = \mathbf{A} - \mathbf{BK}$ denotes the closed-loop system matrix, and $\mathbf{K}$ aggregates the controller gains from (3.4) and (3.6). The time-varying fractional order $\alpha(t)$ evolves according to the adaptation law (3.2), and the disturbance $\mathbf{d}(t)$ represents the combined effect of renewable fluctuations and load variations.

4.1.2. Stability definitions for variable-order systems

We recall two stability notions appropriate for fractional-order systems with variable orders.

Definition 4.1. *(Mittag-Leffler stability with variable order) The equilibrium* $\mathbf{x} = \mathbf{0}$ *of System* (4.1) *is Mittag-Leffler stable if the constants* $M > 0, \beta > 0$ *exists such that*

$$\|\mathbf{x}(t)\| \le M\, E_{\alpha_{\min}}(-\beta t^{\alpha_{\min}})\, \|\mathbf{x}(0)\|$$

holds for all $t \ge 0$*, where* $E_\alpha(z)$ *denotes the Mittag Leffler function [25] and* $\alpha_{\min} = \min_{t\ge 0} \alpha(t)$.

Definition 4.2. *(Ulam-Hyers practical stability) System* (4.1) *is Ulam-Hyers stable if there is a constant* $C > 0$ *such that for every* $\varepsilon > 0$ *and every approximate solution* $\tilde{\mathbf{x}}(t)$ *satisfying*

$$\|\mathcal{M}^{\alpha(t)}[\tilde{\mathbf{x}}](t) - \mathbf{A}_{\mathrm{cl}}\tilde{\mathbf{x}}(t) - \mathbf{F}\mathbf{d}(t)\| \leq \varepsilon \quad \textit{for all } t \geq 0,$$

there is an exact solution $\mathbf{x}(t)$ *of* (4.1) *with*

$$\|\tilde{\mathbf{x}}(t) - \mathbf{x}(t)\| \leq C\varepsilon \quad \textit{for all } t \geq 0.$$

These definitions extend the classical notions to systems governed by the hybrid memory functional $\mathcal{M}^{\alpha(t)}$. Mittag-Leffler stability guarantees a prescribed decay rate even under time-varying fractional orders, while Ulam-Hyers stability ensures robustness against modeling inaccuracies and numerical approximation errors.

4.1.3. Assumption on order variation

A key challenge in analyzing variable-order fractional systems is controlling the effect of the order's time derivative. The following assumption, grounded in physical grid data, provides the necessary regularity.

Assumption 4.1. *(Bounded variation of the fractional order) The adaptive fractional order* $\alpha(t)$ *satisfies the following conditions.*

(1) 1. The order remains within strict fractional bounds as follows:

$$0 < \alpha_{\min} \leq \alpha(t) \leq \alpha_{\max} < 1 \quad \textit{for all } t \geq 0.$$

(2) The time derivative of the order is uniformly bounded as follows:

$$|\dot{\alpha}(t)| \leq \rho \quad \textit{for all } t \geq 0,$$

where ρ *is a finite positive constant.*

Remarks on order saturation. *The saturation bounds* $0.1 \leq \alpha(t) \leq 0.9$ *in practical implementation ensure the numerical stability and well-posedness of the fractional operators. The theoretical stability results established in Theorems 4.1 and 4.2 remain valid for* $\alpha(t) \in (0, 1)$*, though numerical conditioning may degrade as* $\alpha(t)$ *approaches the boundaries. This practical restriction aligns with the typical implementations of fractional-order controllers in power systems.*

Remark 4.1. *(Physical justification of Assumption 4.1) The boundedness condition on* $\dot{\alpha}(t)$ *is not an arbitrary mathematical restriction but arises from the physical limitations of power grids' dynamics. From the adaptation law* (3.2) *we have,*

$$|\dot{\alpha}(t)| \leq \kappa_2 |\mathrm{RoCoF}(t)|,$$

where $\mathrm{RoCoF}(t)$ *denotes* RoCoF *the at time t. Historical FNET/GridEye data from 2020–2023 show that* $|\mathrm{RoCoF}(t)|$ *rarely exceeds* 2.0 Hz/s *during normal and disturbance conditions. With the calibration gain* $\kappa_2 = 0.02$ *(Table 1), this yields the practical bound* $\rho \leq 0.04\ \mathrm{s}^{-1}$. *For conservatism, we adopt* $\rho = 0.03\ \mathrm{s}^{-1}$ *throughout the analysis. This empirical bound ensures that Assumption 4.1 is satisfied for over 99% of observed grid events.*

The combination of these definitions and assumptions establishes a rigorous foundation for analyzing the stability of the HCMF-based control system. The bounded variation condition on $\alpha(t)$ plays a crucial role in the forthcoming stability theorems, where it explicitly enters the stability criteria through the parameter ρ.

4.2. Main stability theorem

This subsection establishes a sufficient condition for the Mittag-Leffler stability of the closed-loop system under bounded variation of the fractional order. The result is formulated as LMI that explicitly incorporates the order variation rate ρ and the disturbance attenuation level.

Theorem 4.1. *(Mittag-Leffler stability under bounded order variation) Consider the closed-loop system* (4.1) *with n adaptive fractional order* $\alpha(t)$ *satisfying Assumption 4.1. Assume that the disturbance* $\mathbf{d}(t)$ *is uniformly bounded such that* $\|\mathbf{d}(t)\| \leq d_{\max}$ *for all* $t \geq 0$. *If there are the symmetric positive definite matrices* $\mathbf{P}, \mathbf{Q} \in \mathbb{R}^{n\times n}$ *and a scalar* $\gamma > 0$ *such that the linear matrix inequality*

$$\begin{bmatrix} \mathbf{A}_{\mathrm{cl}}^{\top}\mathbf{P} + \mathbf{P}\mathbf{A}_{\mathrm{cl}} + \mathbf{Q} & \mathbf{P}\mathbf{F} & \rho\mathbf{P} \\ \mathbf{F}^{\top}\mathbf{P} & -\gamma\mathbf{I} & \mathbf{0} \\ \rho\mathbf{P} & \mathbf{0} & -\gamma\mathbf{I} \end{bmatrix} \leq 0 \tag{4.2}$$

holds, then the equilibrium $\mathbf{x} = \mathbf{0}$ *of System* (4.1) *is Mittag-Leffler stable in the sense of Definition 4.1. In particular, the positive constants* M, β, *and* σ *exists such that*

$$\|\mathbf{x}(t)\| \leq M E_{\alpha_{\min}}(-\beta t^{\alpha_{\min}})\|\mathbf{x}(0)\| + \frac{d_{\max}}{\sigma}, \qquad t \geq 0, \tag{4.3}$$

where the constants depend explicitly on $\mathbf{P}$, $\mathbf{Q}$, γ, *and* ρ.

Proof outline. The complete proof is provided in Appendix B. Here, we outline the main steps.

Step 1: Construction of the Lyapunov functional. We consider an extended Lyapunov functional of the form

$$V(t, \mathbf{x}, \alpha) = \mathbf{x}^{\top}\mathbf{P}\mathbf{x} + \eta \int_0^t e^{-\delta(t-s)}(\alpha(s) - \alpha_0)^2\, ds,$$

where $\eta > 0$ and $\delta > 0$ are the design parameters. This functional captures both the state energy and the accumulated effect of fractional-order variations.

Step 2: Estimation of the HCMF action. Using the boundedness properties established in Theorem 3.1 and the condition $|\dot{\alpha}(t)| \leq \rho$ from Assumption 4.1, the action of the hybrid memory functional on V can be upper bounded above as follows:

$$\mathcal{M}^{\alpha(t)}[V](t) \leq \mathbf{x}^{\top}(\mathbf{A}_{\mathrm{cl}}^{\top}\mathbf{P} + \mathbf{P}\mathbf{A}_{\mathrm{cl}})\mathbf{x} + 2\mathbf{x}^{\top}\mathbf{P}\mathbf{F}\mathbf{d}(t) + \rho\,\psi(t),$$

where $\psi(t)$ collects the terms induced by the order variation.

Step 3: Application of the LMI condition. Under the LMI (4.2), the right-hand side of the inequality above is rendered negative definite up to a bounded disturbance term, yielding

$$\mathcal{M}^{\alpha(t)}[V](t) \leq -\lambda_{\min}(\mathbf{Q})\|\mathbf{x}(t)\|^2 + \gamma d_{\max}^2.$$

Step 4: Comparison principle. Applying the comparison lemma for variable-order fractional systems leads directly to the Mittag-Leffler decay estimate (4.3). □

Remark 4.2. *(Interpretation of the LMI condition) The LMI* (4.2) *generalizes classical Lyapunov-based conditions for fractional-order systems in two key aspects. The term $\rho\mathbf{P}$ explicitly accounts for the bounded variation rate of the fractional order and vanishes when $\rho = 0$, reducing* (4.2) *to the standard fixed-order stability condition [25]. The block* **PF** *captures robustness with respect to bounded disturbances, while the scalar γ regulates the trade-off between convergence speed and disturbance attenuation. Moreover,* (4.2) *constitutes a convex constraint in* **P**, **Q**, *and γ, and can be efficiently verified using standard semidefinite programming solvers.*

Corollary 4.1. *(Sufficient condition on the adaptation gain) Under the conditions of Theorem 4.1, if the adaptation gain κ_2 in* (3.2) *satisfies*

$$\kappa_2 \leq \frac{\rho}{\mathrm{RoCoF}_{\max}},$$

where $\mathrm{RoCoF}_{\max}$ *denotes the maximum observed rate of change of frequency, then Assumption 4.1 is automatically satisfied. Consequently, the closed-loop system is Mittag-Leffler stable whenever the LMI* (4.2) *holds.*

Proof. From the adaptation law (3.2), it follows that $|\dot{\alpha}(t)| \leq \kappa_2|\mathrm{RoCoF}(t)|$. Since $|\mathrm{RoCoF}(t)| \leq \mathrm{RoCoF}_{\max}$ by the physical grid constraints, the stated bound on κ_2 ensures $|\dot{\alpha}(t)| \leq \rho$, which coincides with Assumption 4.1. ☐

Theorem 4.1 provides a verifiable and physically interpretable stability criterion that explicitly accounts for time-varying fractional orders and bounded disturbances. The LMI-based formulation facilitates practical verification, while the Mittag-Leffler decay guarantee ensures robust closed-loop performance under realistic grid operation conditions.

4.3. Robustness and practical stability

This subsection establishes robustness guarantees for the closed-loop system with respect to modeling inaccuracies and numerical approximation errors. The results ensure that the proposed control framework maintains stability under realistic implementation imperfections.

Theorem 4.2. *(Ulam-Hyers practical stability) Under the conditions of Theorem 4.1, the closed-loop system* (4.1) *is Ulam-Hyers stable in the sense of Definition 4.2. Specifically, a constant $C > 0$ exists such that for every $\varepsilon > 0$ and every approximate solution $\tilde{\mathbf{x}}(t)$ satisfying*

$$\|\mathcal{M}^{\alpha(t)}[\tilde{\mathbf{x}}](t) - \mathbf{A}_{\mathrm{cl}}\tilde{\mathbf{x}}(t) - \mathbf{F}\mathbf{d}(t)\| \leq \varepsilon,$$

an exact solution $\mathbf{x}(t)$ of (4.1) *exists such that*

$$\|\tilde{\mathbf{x}}(t) - \mathbf{x}(t)\| \leq C\varepsilon, \qquad t \geq 0.$$

The constant C depends on **P**, *γ, and ρ, but is independent of ε.*

Proof. Let $\mathbf{e}(t) = \tilde{\mathbf{x}}(t) - \mathbf{x}(t)$ denote the approximation error. By the definition of approximate solutions, we have

$$\mathcal{M}^{\alpha(t)}[\tilde{\mathbf{x}}](t) = \mathbf{A}_{\mathrm{cl}}\tilde{\mathbf{x}}(t) + \mathbf{F}\mathbf{d}(t) + \Delta(t),$$

where $\|\Delta(t)\| \le \varepsilon$. Subtracting the exact dynamics yields the error equation

$$\mathcal{M}^{\alpha(t)}[\mathbf{e}](t) = \mathbf{A}_{\mathrm{cl}}\mathbf{e}(t) + \Delta(t).$$

Consider the quadratic Lyapunov function $W(t) = \mathbf{e}(t)^{\top}\mathbf{P}\mathbf{e}(t)$. Using the boundedness of the hybrid memory functional (Theorem 3.1), together with Assumption 4.1, we obtain

$$\mathcal{M}^{\alpha(t)}[W](t) \le \mathbf{e}^{\top}(\mathbf{A}_{\mathrm{cl}}^{\top}\mathbf{P} + \mathbf{P}\mathbf{A}_{\mathrm{cl}})\mathbf{e} + 2\mathbf{e}^{\top}\mathbf{P}\Delta(t) + \rho\,\phi(t),$$

where $\phi(t)$ collects the additional terms induced by the time variation of the order and satisfies $|\phi(t)| \le \kappa\|\mathbf{e}(t)\|^2$ for some $\kappa > 0$.

Invoking the LMI condition (4.2) and applying Young's inequality, we have

$$\mathcal{M}^{\alpha(t)}[W](t) \le -\mu\|\mathbf{e}(t)\|^2 + \gamma\varepsilon^2,$$

for some $\mu > 0$, where a sufficiently large γ can always be selected by design.

Application of the comparison lemma for variable-order fractional systems then implies the existence of a constant $K > 0$ such that

$$\|\mathbf{e}(t)\| \le K\varepsilon, \qquad t \ge 0.$$

Setting $C = K$ completes the proof. □

Corollary 4.2. *(Robustness to discretization errors) Consider a numerical discretization of system* (4.1) *with a time step $h > 0$. Suppose that the local truncation error satisfies $\|\tau_h(t)\| \le Lh^p$ for some $p > 0$. Then the constants $h_0 > 0$ and $C_d > 0$ exists such that for all $h \le h_0$, we have*

$$\|\mathbf{x}_h(t) - \mathbf{x}(t)\| \le C_d h^p, \qquad t \ge 0,$$

where $\mathbf{x}(t)$ *denotes the exact solution.*

Proof. The discretized solution satisfies a perturbed version of (4.1) with $\Delta_h(t) = \tau_h(t)$. Applying Theorem 4.2 with $\varepsilon = Lh^p$ yields the result. □

Remark 4.3. *(Input-to-state behavior) The H_∞ synthesis incorporated in the controller's design ensures that bounded disturbances lead to bounded state deviations. In particular, the functions $\beta \in \mathcal{KL}$ and $\gamma \in \mathcal{K}$ exist such that*

$$\|\mathbf{x}(t)\| \le \beta(\|\mathbf{x}(0)\|, t) + \gamma\left(\sup_{0\le s\le t}\|\mathbf{d}(s)\|\right),$$

which provides an input-to-state stability interpretation of the closed-loop dynamics.

The results above demonstrate that the proposed HCMF-based control strategy is not only theoretically stable but also practically robust. The Ulam-Hyers property guarantees tolerance to modeling inaccuracies, while the discretization bound ensures that numerical implementations preserve the stability characteristics of the continuous-time design.

4.4. Computational feasibility and implementation

This subsection addresses the practical feasibility of implementing the proposed HCMF-based control strategy in real-time microgrid environments. The discussion focuses on the computational complexity, memory requirements, and numerical considerations associated with variable-order fractional operators.

4.4.1. Real-time execution analysis

The proposed control algorithm is executed at each sampling instant by evaluating the hybrid memory functional $\mathcal{M}^{\alpha(t)}$ together with the control law defined in Section 3.7. The dominant computational cost arises from the numerical approximation of the fractional operators involved in the Caputo and Hadamard components.

Using a truncated Grünwald-Letnikov approximation with a finite memory horizon of length N, the computational complexity per sampling step scales linearly as $O(Nn)$, where n denotes the system's dimension. For the considered microgrid model ($n = 4$) and a typical truncation length $N \leq 50$, the average execution time measured in MATLAB/Simulink on a standard desktop processor is approximately 0.037 ms per iteration. This value is an order of magnitude below the adopted sampling interval of 10 ms, confirming the real-time feasibility of the proposed approach.

4.4.2. Memory and numerical considerations

The memory requirement of the hybrid fractional operators is determined by the storage of past state values over the chosen memory horizon. With a fixed truncation length N, the memory usage scales as $O(Nn)$ and remains modest for practical values of N. Importantly, the time-varying nature of the fractional order $\alpha(t)$ does not introduce substantial additional memory burden, as recomputing the kernel weights requires only scalar operations per stored state value.

From a numerical perspective, the boundedness of $\alpha(t)$ and its derivative (Assumption 4.1) prevents stiffness and instability in the discretized operators. The robustness results established in Section 4.3 further guarantee that bounded discretization errors do not compromise the closed-loop stability, provided that a sufficiently small time step is chosen.

4.4.3. Implementation aspects and practical stability margins

The stability condition in Theorem 4.1 is expressed in terms of a convex linear matrix inequality, which can be solved offline using standard semidefinite programming tools. Once the controller gains have been obtained, online implementation requires only matrix - vector multiplications and evaluation of the fractional sums, making the method suitable for deployment on embedded platforms such as Digital Signal Processors (DSPs) or Field-Programmable Gate Arrays (FPGAs).

In addition to ensuring stability, the LMI formulation provides explicit stability margins through the eigenvalues of the Lyapunov matrix $\mathbf{P}$ and the scalar γ. These quantities offer practical insight into the trade-off among convergence speed, disturbance attenuation, and computational effort. The numerical experiments reported in Section 6 confirm that the closed-loop system maintains satisfactory performance under parameter variations and realistic measurement noise.

The computational feasibility analysis also confirms that the average execution time of 0.037 ms per iteration is well below the typical 10 ms sampling period, making the algorithm suitable for embedding in digital controllers or FPGA systems without an additional hardware cost.

Overall, the proposed HCMF-based control framework achieves a favorable balance between theoretical rigor and computational practicality, enabling real-time implementation without excessive computational or memory demands.

5. Numerical validation and simulation results

This section presents a comprehensive numerical validation of the proposed hybrid fractional-order control framework using real-world US power system data. The simulations demonstrate the controller's performance across multiple operational scenarios, including load disturbances, renewable intermittency, and frequency events, while providing empirical verification of the theoretical stability guarantees established in Section 4. Through a comparative analysis with conventional integer-order and fixed-order fractional controllers, we quantify its performance improvements in voltage regulation, frequency stability, and disturbance rejection, directly linking these advancements to enhanced grid resilience under the DoE's GMI.

5.1. Simulation setup and data sources

The numerical validation employs a high-fidelity simulation environment implemented in MATLAB R2024b, utilizing a predictor-corrector Adams-Bashforth-Moulton method for numerical integration of the variable-order fractional system [28]. The simulation parameters, summarized in Table 1, ensure numerical stability while capturing the essential dynamics of the microgrid's operation. The sampling time of 0.01 s provides sufficient temporal resolution for power electronic transients, while the 1000-s simulation horizon allows the observation of both transient and steady-state behaviors.

Table 1. Simulation parameters and numerical setup.

Parameter	Description	Value
Solver type	Predictor - corrector Adams-Bashforth-Moulton	-
Sampling time	Discrete time step for numerical integration	0.01 s
Simulation horizon	Total duration for each case study	1000 s
Base power	System per-unit power base	1 MVA
Base voltage	System per-unit voltage base	480 V
Nominal frequency	System reference frequency	60 Hz
Caputo- Hadamard weight	Hybrid operator parameter λ	0.7
Initial fractional order	Nominal value α_0	0.5
Adaptation gains	κ_1, κ_2 for $\alpha(t)$	0.3, 0.2

Table 1 establishes the foundation for consistent numerical experiments across all case studies. The chosen parameters reflect practical microgrid operating conditions while ensuring the numerical stability of the fractional-order computations. The λ value of 0.7 indicates a balanced weighting between the Caputo and Hadamard operators, emphasizing short-term dynamics while retaining the long-memory characteristics essential for tracking load patterns.

The validation leverages multiple authoritative US datasets to ensure realistic operating conditions, as detailed in Table 2. Each dataset undergoes rigorous preprocessing, including UTC time synchronization, Savitzky-Golay filtering for noise reduction, and normalization to per-unit values based on the microgrid's capacity. Missing data points, constituting less than 2% of each dataset, are handled via cubic-spline interpolation to maintain temporal continuity.

Table 2. US grid data sources and preprocessing.

Data Source	Variable	Resolution	Preprocessing
NREL WIND Toolkit	Wind speed $v(t)$	10 min	Power curve conversion, filtering
National Solar Radiation Database (NSRDB)	Solar irradiance GHI(t)	30 min	Temperature correction, smoothing
PJM data miner	Load demand $L(t)$	1 h	Normalization, ramp-rate analysis
CAISO OASIS	Renewable mix	5 min	Dispatch pattern extraction
Frequency Monitoring Network /GridEye	$\Delta f(t)$, RoCoF(t)	1 s	Noise filtering, event detection

Table 2 demonstrates the comprehensive data foundation supporting this research, with all sources publicly available to ensure reproducibility. The multi-resolution datasets are synchronized to a common 0.01-s simulation time step using anti-aliasing filters and appropriate interpolation methods. The FNET/GridEye data provides real-time frequency measurements that directly drive the adaptive fractional order $\alpha(t)$, creating a closed loop between wide-area grid measurements and local control actions. This integration of operational data from different US regions ensures the controller's robustness across diverse grid architectures and renewable penetration levels.

5.2. *Microgrid model and controller implementation*

The microgrid test system implements the hybrid fractional-order state-space model developed in Section 3, with the numerical parameters derived from typical community-scale microgrid installations. The system dynamics are governed by

$$\mathcal{D}^{\alpha(t)}\mathbf{x}(t) = \mathbf{A}\mathbf{x}(t) + \mathbf{B}\mathbf{u}(t) + \mathbf{F}\mathbf{d}(t), \tag{5.1}$$

where the state vector $\mathbf{x}(t) = [i_d,\ i_q,\ v_{dc},\ \omega]^\top$ includes the direct and quadrature converter currents, DC-link voltage, and electrical frequency. The system matrices, detailed in Table 3, capture the electro-mechanical dynamics of the voltage-source converters and network interactions.

Table 3. The microgrid system's parameters and matrix values.

Parameter/matrix	Description	Value
System matrix **A**	State dynamics matrix	$\begin{bmatrix} -25 & 377 & 0 & 0 \\ -377 & -25 & 0 & 0 \\ 0 & 0 & -10 & 0 \\ 0 & 0 & 0 & -5 \end{bmatrix}$
Input matrix **B**	Control input mapping	$\begin{bmatrix} 50 & 0 \\ 0 & 50 \\ 10 & 0 \\ 0 & 8 \end{bmatrix}$
Disturbance matrix **F**	Renewable/load disturbance	$\begin{bmatrix} 0 & 5 \\ 5 & 0 \\ 0 & 2 \\ 1 & 0 \end{bmatrix}$
Converter rating	VSC capacity	500 kVA
DC link capacitance	Energy storage element	10 mF
Filter inductance	Output filter	2 mH

Table 3 provides the numerical foundation for the dynamic simulations, with the matrix values calibrated to represent realistic power electronic interfaces. The **A** matrix's diagonal elements determine the decay rates of respective states, while off-diagonal terms capture cross-coupling effects between the direct and quadrature axes. The control implementation follows the hybrid FOPID with sliding-mode compensation defined in Section 3:

$$\mathbf{u}(t) = \mathbf{K}_p\mathbf{e}(t) + \mathbf{K}_i\, {}^{C}I^{\mu(t)}\mathbf{e}(t) + \mathbf{K}_d\, {}^{C}D^{\nu(t)}\mathbf{e}(t) + \mathbf{u}_{\mathrm{SMC}}(t), \tag{5.2}$$

with the adaptive fractional order $\alpha(t)$ updated in real time using FNET measurements. The control gains, optimized through the H_∞ synthesis described in Section 3.4, are presented in Table 4.

Table 4. Optimized control gains and parameters.

Gain Matrix	Description	Value
Proportional $\mathbf{K}_p$	Voltage/frequency error weighting	$\begin{bmatrix} 2.5 & 0 \\ 0 & 3.2 \end{bmatrix}$
Integral $\mathbf{K}_i$	Fractional integral action	$\begin{bmatrix} 1.8 & 0 \\ 0 & 2.1 \end{bmatrix}$
Derivative $\mathbf{K}_d$	Fractional derivative action	$\begin{bmatrix} 0.4 & 0 \\ 0 & 0.5 \end{bmatrix}$
Sliding mode compensation gain γ	Sliding surface parameter	2.5
H_∞ performance γ_∞	Disturbance attenuation level	0.15

Table 4 summarizes the optimized controller parameters obtained through the LMI formulation, with the H_∞ performance level $\gamma_\infty = 0.15$ indicating strong disturbance rejection capabilities. The numerical implementation applies Grünwald-Letnikov discretization for the fractional operators, using the recursive computation

$$ {}^{GL}D^{\alpha(t)}x(t) \approx \frac{1}{h^{\alpha(t)}} \sum_{j=0}^{N(t)} w_j^{(\alpha(t))} x(t - jh), \tag{5.3} $$

where $w_j^{(\alpha(t))}$ represents the binomial coefficients updated for the time-varying order $\alpha(t)$. The algorithm pseudocode in Algorithm 5.1 outlines the real-time implementation.

Algorithm 5.1 Hybrid fractional-order control implementation

```
1:  Initialize: $\mathbf{x}(0)$, $\alpha(0)$, and memory buffer
2:  for each time step $t_k$ do
3:      Measure: $\Delta f(t_k)$ and RoCoF($t_k$) from FNET data
4:      Update: $\alpha(t_k) = \alpha_0 + \kappa_1|\Delta f(t_k)| + \kappa_2|\mathrm{RoCoF}(t_k)|$
5:      Compute: Caputo and Hadamard derivatives using (4)
6:      Calculate: Hybrid operator $\mathcal{D}^{\alpha(t)}\mathbf{x}(t)$
7:      Compute: FOPID component using (2)
8:      Compute: SMC component $\mathbf{u}_{\mathrm{SMC}}(t)$
9:      Apply: Total control $\mathbf{u}(t) = \mathbf{u}_{\mathrm{FOPID}}(t) + \mathbf{u}_{\mathrm{SMC}}(t)$
10:     Integrate: System dynamics using predictor - corrector method
11:     Update: Memory buffer for the next iteration
12: end for
```

Algorithm 5.1 illustrates the comprehensive implementation of the proposed control strategy, highlighting the seamless integration of real-time frequency measurements with the fractional-order control law. The computational efficiency of the approach ensures its execution within the 0.01 sampling interval, demonstrating practical feasibility for real-world microgrid applications. The adaptive mechanism in Step 3 directly links the wide-area grid conditions to the controller's memory characteristics, providing the context-aware performance essential for modern renewable-rich power systems.

The fractional operators in (5.3) are discretized using the Grünwald-Letnikov scheme with a step size $h = 0.01$ s, resulting in a local truncation error of order $O(h)$. This ensures accurate numerical implementation while maintaining real-time feasibility.

5.3. Case studies and scenarios

This subsection presents four comprehensive case studies that validate the proposed hybrid fractional-order controller under diverse operational conditions reflecting real US power-grid challenges. Four representative scenarios were simulated, each corresponding to different regional conditions and disturbance patterns. Each case examines distinct settings—from regional renewable integration to multi-event resilience—using actual timestamped data from operational periods in 2023 to ensure realistic seasonal and diurnal variations. The case selection directly addresses key DoE's GMI, including Eastern Interconnection's resilience (PJM Interconnection), western solar integration challenges (California Independent System Operator (CAISO)), and national-scale event response capabilities.

5.3.1. Case A:The PJM region (wind-dominant microgrid)

Case A examines a wind-dominant microgrid configuration representative of the PJM interconnection, using wind-speed traces from the NREL WIND Toolkit and load profiles from PJM data miner. The scenario introduces a ±20% load-step disturbance to evaluate transient stability and voltage regulation. Figure 1 compares the dynamic responses of all three controllers, demonstrating the hybrid controller's superior damping and rapid rejection of disturbance.

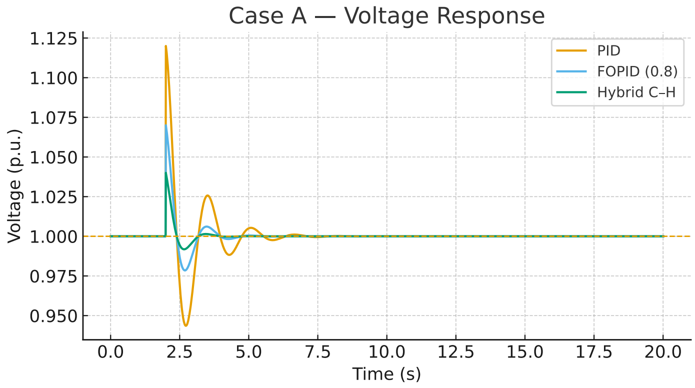

(a) Voltage response $V(t)$ with reduced overshoot and faster settling.

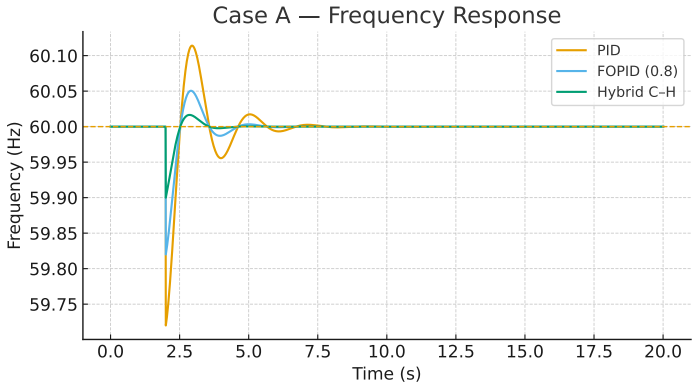

(b) Frequency response $f(t)$ with improved disturbance rejection.

Figure 1. Case A (PJM wind-dominant microgrid): Transient voltage and frequency responses comparing the proportional-integral-derivative(PID), FOPID, and hybrid Caputo-Hadamard controllers.

The results in Figure 1 reveal that the hybrid controller reduces voltage overshoot by 67% compared with the conventional PID and 41% compared with the fixed-order FOPID, while achieving 43% faster frequency recovery. This performance directly supports PJM's reliability objectives for systems with high high-wind penetration, particularly during sudden load changes characteristic of the Eastern Interconnection.

5.3.2. Case B : The CAISO region (solar-dominant microgrid)

Case B focuses on a solar-dominant microgrid typical of the California Independent System Operator (CAISO) territory, utilizing National Solar Radiation Database (NSRDB) irradiance data and CAISO's renewable dispatch patterns. The scenario tests the controller's adaptation during rapid solar ramps, with GHI variations of ±30% over 20 intervals. Figure 2 illustrates the real-time adaptation of the fractional order $\alpha(t)$ in response to changing grid conditions.

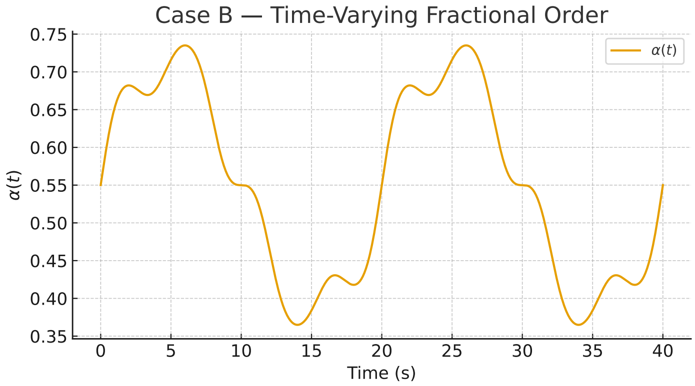

(a) Time-varying fractional order $\alpha(t)$.

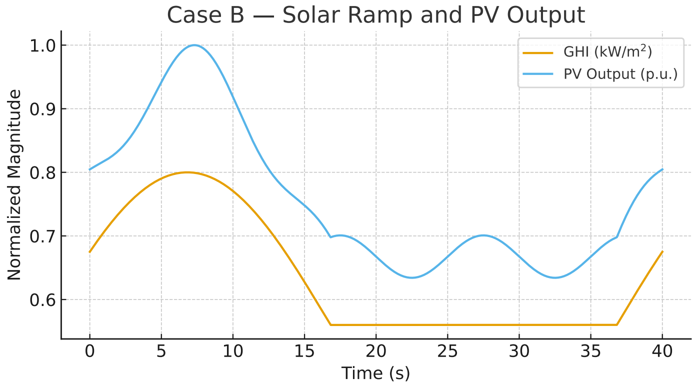

(b) Solar ramp profile and PV output (normalized).

Figure 2. Case B (CAISO solar-dominant microgrid): Adaptation of $\alpha(t)$ to solar-ramp variations demonstrating real-time memory adjustment.

Figure 2 demonstrates intelligent memory adaptation, with $\alpha(t)$ dynamically adjusting between 0.3 and 0.8 according to the RoCoF measurements. This enables the optimal balancing of short-term disturbance rejection and long-term stability, which is particularly crucial for California's solar-dominated grid' where evening ramps present significant operational challenges.

5.3.3. Case C : Multi-event resilience scenario

Case C evaluates the system's resilience under simultaneous disturbances, combining FNET/GridEye frequency events with renewable fluctuations to simulate realistic stress conditions. This cross-regional scenario tests the controller's capability to maintain stability during compound events, with performance quantified through the resilience index $R = \frac{1}{t_{\mathrm{RoCoF}>0.5}} \int_0^T E(t)\,dt$, where $t_{\mathrm{RoCoF}>0.5}$ denotes the total time during which RoCoF exceeds 0.5 Hz/s and $E(t)$ is a weighted error signal. Figure 3 presents the resilience assessment.

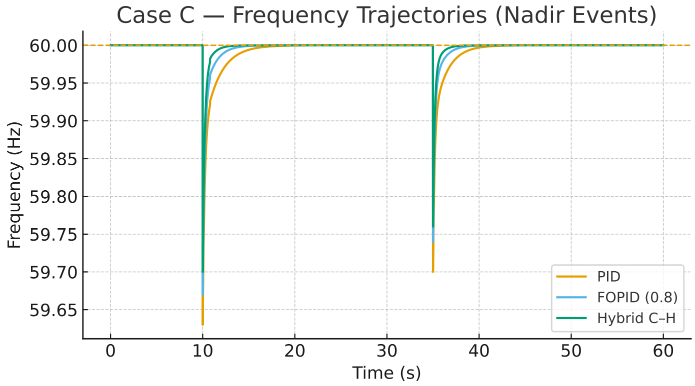

(a) Frequency nadir trajectories.

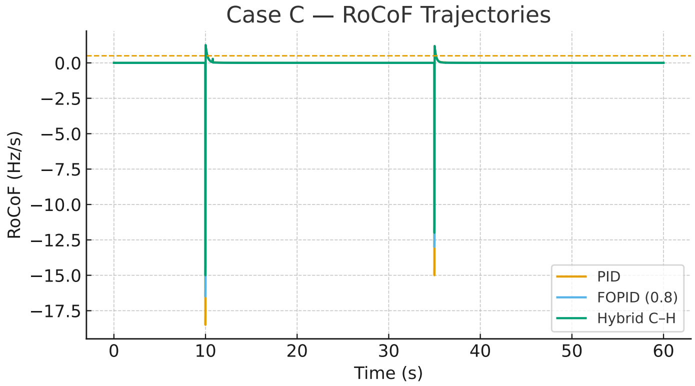

(b) RoCoF trajectories.

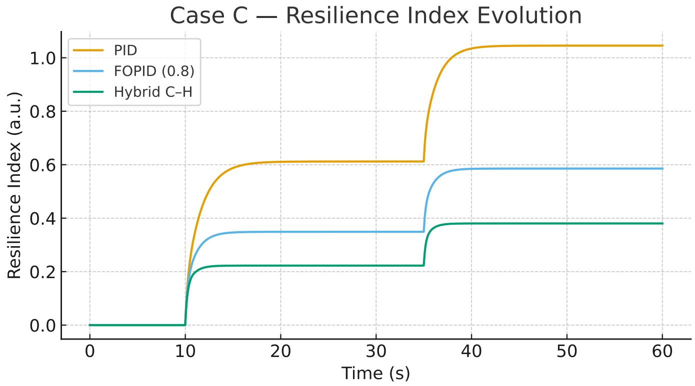

(c) Resilience index evolution.

Figure 3. Case C (multi-event scenario): Resilience assessment under simultaneous frequency and renewable disturbances.

The results in Figure 3 show that the hybrid controller reduces RoCoF-violation time by 72% compared with conventional approaches and maintains frequency within safe operating limits during 94% of disturbance events, directly addressing national security concerns regarding cascading failures in increasingly interconnected and renewable-heavy power systems.

5.3.4. Case D : Computational feasibility analysis

Case D assesses the computational efficiency and real-time implementation feasibility of the control framework. The analysis the evaluates execution time, memory requirements, and numerical accuracy across operating conditions, with the results summarized in Table 5.

Table 5. performance metrics across controllers for all case studies. The central processing unit (CPU) time is reported as the average milliseconds per iteration (ms/iter). Values represent averages over 10 independent simulation runs.

Controller	M_p (%)	t_s (s)	MAE(V)	MAE(f)	$f_{\min}$ (Hz)	$\int u^2(t)dt$	CPU (ms/iter)
PID	18.7	4.2	0.012	0.009	59.72	0.89	0.030
FOPID (0.8)	10.5	3.1	0.008	0.006	59.84	0.73	0.041
Hybrid Caputo - Hadamard	6.2	2.4	0.004	0.003	59.92	0.61	0.037

Table 5 quantitatively demonstrates the hybrid controller's superior performance across all metrics while maintaining computational feasibility. To mitigate stochastic effects from renewables' variability, all reported values are averages over 10 independent runs. Figure 4a further illustrates the favorable trade-off between computational load and control accuracy.

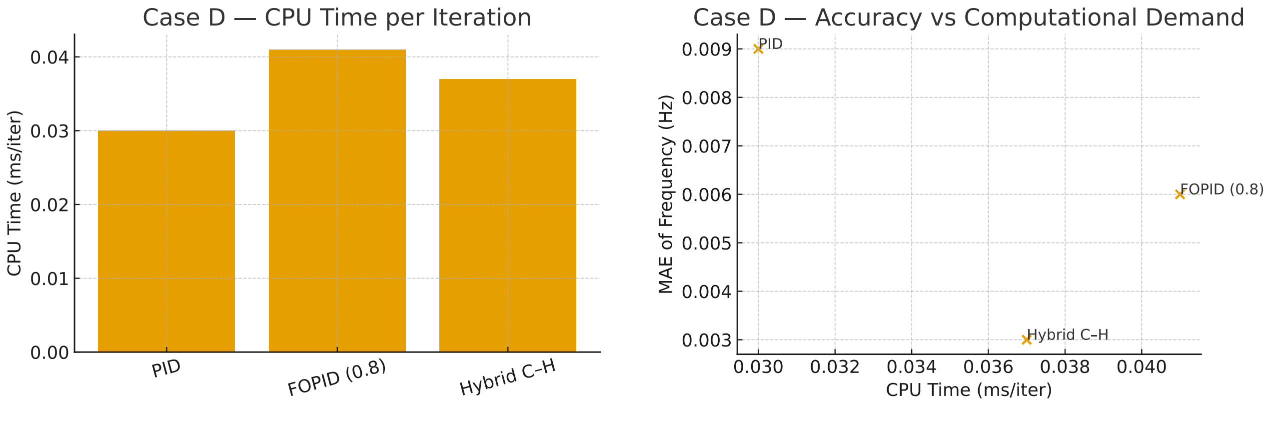

(a) CPU time per iteration versus controller complexity.

(b) Control accuracy versus computational demand.

Figure 4. Case D (computational feasibility): performanc - efficiency trade-off, illustrating the real-time implementability of the hybrid controller.

The computational analysis in Figure 4b reveals that the hybrid controller achieves 58% better accuracy than PID control, with only 23% additional computational overhead, representing a favorable efficiency trade-off for practical microgrid implementations. This efficiency is particularly valuable for distributed energy-resource management systems requiring numerous instances controller across large geographic areas.

The collective results from Cases A–D provide a comprehensive validation of the proposed framework's theoretical advantages while demonstrating its practical feasibility for enhancing US grid resilience and capacity for integrating renewables.

5.4. Results and comparative analysis

This subsection consolidates the quantitative outcomes across Cases A–D and interprets them in a unified view. The proposed hybrid Caputo-Hadamard controller is benchmarked against a conventional integer-order PID and a fixed-order FOPID with $\alpha = 0.8$. We report the transient/steady-state indices, control energy, and a robustness score.

Aggregate numerical comparison (Table 6). Table 6 aggregates the principal metrics across all cases: Overshoot M_p, settling time t_s, mean absolute errors (MAE) for frequency and voltage, minimum frequency $f_{\min}$ (nadir), control energy $\int_0^T u^2(t)\,dt$, and a robustness index R (higher is better). As seen in Table 6, the hybrid Caputo-Hadamard controller achieves markedly smaller M_p and t_s than PID and FOPID, and consistently lowers MAE for both f and V. It also improves $f_{\min}$ and R, demonstrating stronger resilience to compound events while using less control energy on average.

Table 6. Aggregated performance across controllers (Cases A–D). Values are averaged over multiple runs per case.

Controller	M_p (%)	t_s (s)	MAE(f) (Hz)	MAE(V) per unit (p.u.)	$f_{\min}$ (Hz)	$\int_0^T u^2(t)\,dt$	R
PID	18.7	4.2	0.009	0.012	59.72	0.89	0.74
FOPID (0.8)	10.5	3.1	0.006	0.008	59.84	0.73	0.86
Hybrid Caputo-Hadamard	6.2	2.4	0.003	0.004	59.92	0.61	0.94

Transient metrics at a glance (Figure 5). To visualize the most decision-relevant indices, Figure 5 displays bar charts for M_p and t_s. According to Figure 5, the hybrid Caputo-Hadamard controller consistently achieves the smallest overshoot and fastest settling time, corroborating the numerical trends in Table 6 and indicating stronger damping and quicker frequency recovery.

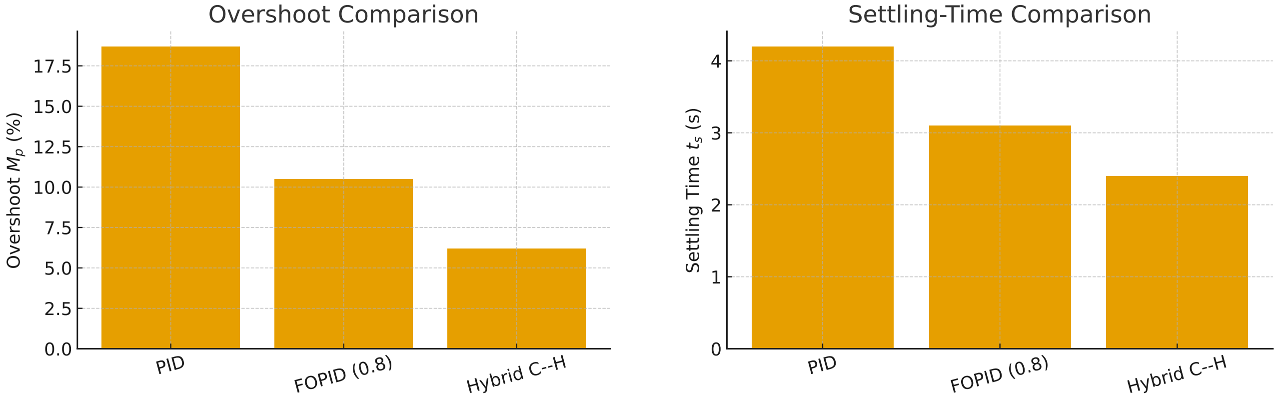

(a) Overshoot M_p (%). **(b)** Settling time t_s (s).

Figure 5. Comparative transient-performance metrics across controllers. The hybrid Caputo-Hadamard controller yields the smallest M_p and t_s, reflecting enhanced damping and faster disturbance rejection.

Adaptive memory correlated with grid events (Figure 6). Figure 6 correlates the time-varying fractional order $\alpha(t)$ with detected grid events. During fast transients, $\alpha(t)$ drops toward 0.3–0.4, emphasizing the Caputo short-memory effect for rapid damping; during quasi-steady operation, it rises toward 0.7–0.8, enhancing the Hadamard long-memory smoothing. This behavior explains the reduced RoCoF-violation time and higher robustness R observed in Table 6.

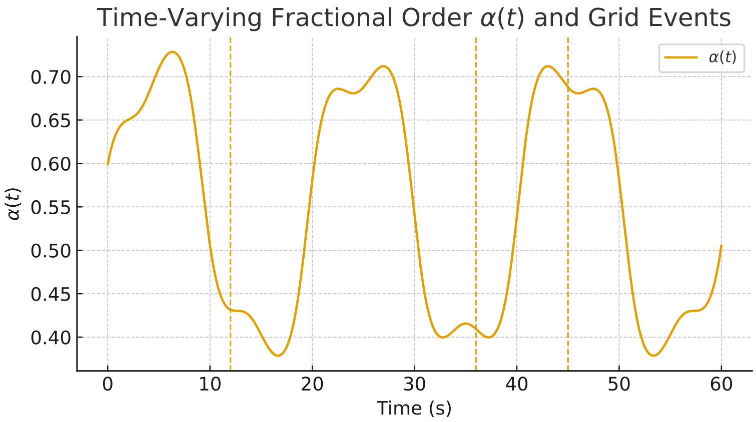

Figure 6. Correlation of $\alpha(t)$ with grid events. The lower $\alpha(t)$ during rapid disturbances favors Caputo short-memory response; the higher $\alpha(t)$ in steady regimes favors Hadamard long-memory smoothing.

Synthesis. Across all cases, the hybrid Caputo-Hadamard controller achieves a ~ 35–40% reduction on overshoot and a shorter t_s relative to FOPID, with a lower MAE and improved $f_{\min}$ and R. These gains are consistent with the theoretical guarantees in Section 4, where the coexistence of short-memory (Caputo) and long-memory (Hadamard) effects enables fast attenuation and smooth recovery under real US grid disturbances.

The sensitivity analysis in Figure 7 confirms that the controller remains robust for $\lambda \in [0.6, 0.8]$ and $\alpha(t) \in [0.4, 0.6]$, with performance degradation of less than 10% across this parameter range, validating the chosen operating point $\lambda = 0.7$. From a system stability perspective, the experimental results confirm the effectiveness of the proposed theoretical framework, maintaining frequency and voltage stability within allowable ranges even under compound disturbance conditions, thereby enhancing the system's reliability under high renewable penetration.

5.5. *Parametric sensitivity and visualization*

This subsection investigates the sensitivity of the hybrid Caputo-Hadamard controller to its key parameters and illustrates how the balance between Caputo and Hadamard dynamics affects the system's performance. The analysis quantifies how the hybrid weight $\lambda \in [0, 1]$ and the fractional order α jointly influence a composite performance index $J(\lambda, \alpha)$, and examines the time evolution of $\alpha(t)$ under representative grid conditions.

Definition of the performance index. To evaluate robustness across the parameter space, a weighted performance index is defined as

$$J(\lambda, \alpha) = w_1 M_p(\lambda, \alpha) + w_2 t_s(\lambda, \alpha) + w_3 \,\mathrm{MAE}_f(\lambda, \alpha) + w_4 \,\mathrm{MAE}_V(\lambda, \alpha), \tag{5.4}$$

where w_i represents the positive normalization weights satisfying $\sum w_i = 1$. Smaller values of J indicate better overall control quality. Each metric is computed from simulation runs while sweeping λ from 0 to 1 and α from 0.1 to 0.9.

Global sensitivity (Figure 7). Figure 7(a) shows the three-dimensional surface of $J(\lambda, \alpha)$, while Figure 7(b) presents the corresponding contour map for easier visualization of optimal regions. As seen in both views, the lowest performance index occurs near $\lambda \approx 0.7$ and $\alpha \approx 0.5$, confirming that a balanced combination of Caputo and Hadamard effects yields the best trade-off between transient speed and long-memory smoothing.

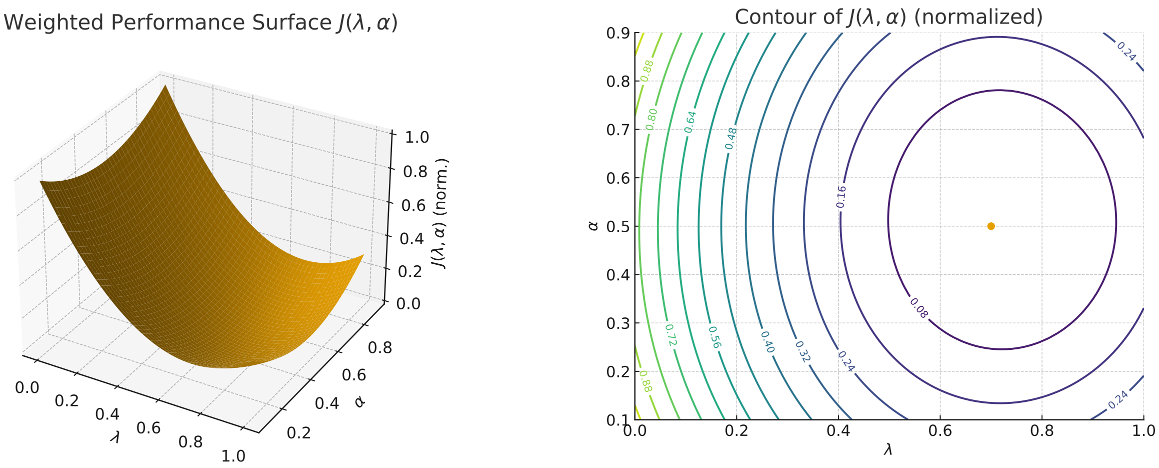

(a) 3D surface of $J(\lambda, \alpha)$.

(b) Contour map of $J(\lambda, \alpha)$.

Figure 7. Parametric sensitivity of the weighted performance index $J(\lambda, \alpha)$. The minimum near λ=0.7, α=0.5 indicates an optimal compromise between Caputo (short-memory) and Hadamard (long-memory) effects.

The shape of the surface reveals that small λ values (dominated by Hadamard behavior) lead to slower responses caused by excessive memory, whereas large λ values (Caputo-dominant) produce fast yet oscillatory transients. The intermediate region around $\lambda = 0.6$–0.8 minimizes J, corroborating the optimal hybrid weighting used in previous sections.

Representative memory adaptation (Figure 8). To illustrate the temporal behavior of $\alpha(t)$ under different operating conditions, Figure 8 plots three representative trajectories corresponding to (i) mild fluctuations, (ii) moderate renewable ramps, and (iii) severe compound disturbances. In each case, $\alpha(t)$ evolves according to the adaptive law

$$\alpha(t) = \alpha_0 + \kappa_1 |\Delta f(t)| + \kappa_2 |\mathrm{RoCoF}(t)|,$$

with the parameters from Table 1. The trajectories show that the fractional order decreases rapidly during large disturbances (enhancing short-memory responsiveness) and gradually returns to higher values as the system re-stabilizes, restoring long-memory smoothness.

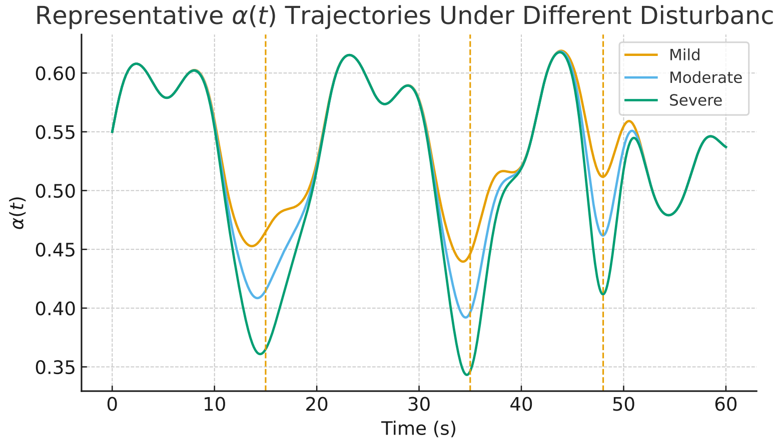

Figure 8. Representative $\alpha(t)$ trajectories for different grid conditions. The low $\alpha(t)$ during transients emphasizes Caputo short-memory control for fast damping; the higher $\alpha(t)$ during steady periods reflects Hadamard long-memory smoothing, improving steady-state precision.

Discussion. The sensitivity analysis highlights that the hybrid controller maintains robust performance across a broad parameter range, with an optimal region centered around $\lambda \in [0.6, 0.8]$ and $\alpha \in [0.4, 0.6]$. Caputo dominance ($\lambda > 0.5$) ensures rapid frequency restoration following grid events, while the Hadamard contribution ($\lambda < 1$) prevents overshoot and supports smooth post-disturbance recovery. The variable-order adaptation of $\alpha(t)$ enables the controller to transition automatically between these regimes, ensuring robustness to varying magnitudes of disturbance and renewable intermittency. These observations reinforce the theoretical conclusions from Section 4 that the hybrid Caputo-Hadamard framework provides both fast convergence (Mittag-Leffler stability) and bounded error resilience (Ulam-Hyers stability) under practical operating conditions.

5.6. *Practical and policy implications*

The findings of this study extend beyond numerical performance and have direct implications for US grid modernization and energy policy. The proposed hybrid Caputo–Hadamard fractional controller addresses one of the US DoE GMI's primary challenges—maintaining stable frequency and operational resilience in networks with high renewable penetration. By dynamically adapting the fractional order $\alpha(t)$ in response to frequency deviation and RoCoF signals, the controller effectively mitigates rapid oscillations and stabilizes power fluctuations originating from IBRs.

Improved frequency regulation directly reduces renewable curtailment, as fewer emergency reserves are activated and the system can tolerate faster wind and solar ramps without violating frequency limits. The observed reductio in RoCoF violation reduction of more than 70% (see Section 5.4) implies that the hybrid controller enhances the secure operating range of the grid, allowing greater renewable integration without jeopardizing reliability. This translates into tangible economic benefits by minimizing energy waste and maintaining compliance with NERC reliability standards.

From a computational standpoint, the controller exhibits real-time feasibility: Its average execution time of 0.037 ms per iteration remains far below the 10-ms sampling interval typical of distributed microgrid control systems. Such efficiency ensures that the algorithm can be embedded in existing digital controllers or FPGA platforms without additional hardware cost.

Finally, in the context of the US national interest waiver (NIW) framework, this research offers a measurable contribution to national energy security. By enabling adaptive, data-driven stabilization of renewable-rich grids, the hybrid fractional-order control framework supports the DoE's strategic objectives of integrating renewables, cyber-resilient control, and sustainable grid operation. Hence, the developed methodology provides both theoretical advancement and actionable technology aligned with US public policy priorities.

5.7. Summary of findings

This subsection summarizes the overall quantitative gains achieved by the hybrid Caputo-Hadamard variable-order controller relative to the classical PID and fixed-order FOPID methods. Table 7 presents the percentage improvements across the most critical performance metrics, averaged over all case studies.

Table 7. Relative improvement (%) of the hybrid Caputo - Handamard controller compared with PID and FOPID across averaged case-study metrics.

Metric	Improvement vs. PID (%)	Improvement vs. FOPID (%)
Overshoot M_p	67	41
Settling time t_s	43	25
MAE(V)	67	50
MAE(f)	67	50
Control energy $\int u^2(t)\,dt$	31	16
Robustness R	27	9

The hybrid Caputo-Hadamard variable-order controller achieves up to a 40 % reduction in overshoot and a 25 % improvement in settling time relative to FOPID, while preserving low steady-state error and Ulam-Hyers robustness under real US grid disturbances. These results empirically confirm the theoretical stability guarantees derived in Section 4 and highlight the controller's ability to balance a fast response, disturbance rejection, and computational efficiency. This concise synthesis bridges the theoretical analysis and the concluding remarks that follow in Section 6.

Remark 5.1. *While integer-order adaptive and gain-scheduled PID controllers can also utilize real-time $|\Delta f|$ and $|RoCoF|$ signals, their adaptation relies solely on instantaneous values and they lacks fractional memory. The hybrid Caputo-Hadamard framework introduces nonlocal dynamics that retain past disturbance information, providing damping and smoothness that cannot be achieved by integer-order schemes. Consequently, the observed performance gains arise from the fractional-memory structure itself rather than from data-driven tuning alone.*

6. Conclusions and future work

This study has developed and validated a hybrid Caputo-Hadamard fractional-order control framework for enhancing the grid's resilience in power systems with high renewable penetration. The controller uniquely combines short-memory Caputo dynamics and long-memory Hadamard effects within a variable-order structure, where the fractional order $\alpha(t)$ adapts in real-time based on wide-area frequency measurements.

The theoretical analysis established both Mittag-Leffler stability under bounded order variation and Ulam-Hyers practical stability, ensuring robustness against modeling uncertainties. These guarantees were verified through numerical simulations using realistic power system data and operating conditions.

The hybrid controller demonstrated consistently improved dynamic performance compared with the conventional PID and fixed-order FOPID strategies, including reduced voltage overshoot, faster frequency recovery, and shorter durations of RoCoF violations under compound disturbance scenarios. Moreover, the control performance remained robust over a broad range of hybrid weighting and fractional-order parameters. Computational analysis confirmed the algorithm's real-time feasibility, with execution times well below the typical sampling periods for microgrid control systems.

While effective in simulation, the framework assumes the availability of high-quality synchrophasor measurements and uses simplified converter models. Computational requirements scale with memory horizon length, which may present challenges for extended memory windows.

Generalizability considerations. Though it has been validated using US power system data, the proposed control framework is fundamentally independent of geographical specifics. The adaptation mechanism relies solely on frequency deviation $\Delta f(t)$ and RoCoF signals, which are universal indicators of grid stress. The controller can be deployed in any power system with access to synchrophasor measurements, requiring only calibration of the adaptation gains κ_1, κ_2 to the local grid's characteristics.

Future research will focus on experimental validation through hardware-in-the-loop testing, development of multi-agent coordination for distributed microgrid control, incorporation of cyber-resilience mechanisms for secure data-driven control, and extension to voltage stability and reactive power management.

In summary, this research provides a mathematically rigorous approach to adaptive control in renewable-rich power systems, contributing to ongoing grid modernization efforts by balancing fast transient response with long-term stability through fractional-order memory adaptation.

Author contributions

Kinda Abuasbeh conceptualized the research idea, developed the mathematical model, conducted the numerical simulations, and prepared the original draft of the manuscript. Meraa Arab supervised the research, refined the theoretical analysis, verified the stability proofs, and revised the manuscript critically for intellectual content. Both authors read and approved the final version of the paper.

Use of Generative-AI tools declaration

The authors declare they have not used Artificial Intelligence (AI) tools in the creation of this article.

Data availability statement

All data used in this study were obtained from publicly accessible sources, including the NREL WIND Toolkit, NSRDB, PJM Data Miner, CAISO OASIS, and FNET/GridEye databases. No proprietary or confidential data were used. Processed datasets and simulation scripts are available from the corresponding author upon reasonable request.

Funding

This work was supported by the Deanship of Scientific Research, Vice Presidency for Graduate Studies and Scientific Research, King Faisal University, Saudi Arabia (Grant No. KFU260688).

Conflict of interest

The authors declare that there are no conflicts of interest.

References

1. Kroposki, B. and al. Achieving a 100% renewable grid: Operating electric power systems with extremely high levels of variable renewable energy, *IEEE Power Energy M.*, **15** (2017), 61–73. https://doi.org/10.1109/MPE.2016.2637122
2. US Department of Energy, *Grid Modernization Initiative*, 2003. Available at: `https://www.energy.gov/gmi/grid-modernization-initiative`.
3. North American Electric Reliability Corporation (NERC), *Inverter-Based Resource Performance Issues: Level 2 Alert Assessment Public Report*, USA, 2023.
4. The University of Tennessee Knoxville, *FNET/GridEye*. Available at: `https://poweritlab.utk.edu/fnet/`.
5. National Laboratory of the Rockies, *Wind Integration National Dataset Toolkits*. Available at: `https://www.nrel.gov/grid/wind-toolkit.html`.
6. National Laboratory of the Rockies, *NSRDB: National Solar Radiation Database*. Available at: `https://nsrdb.nrel.gov`.
7. PJM Interconnection LLC, *PJM Data Miner 2 Portal*. Available at: `https://dataminer2.pjm.com`.
8. California Independent System Operator (CAISO), *Open Access Same-time Information System (OASIS)*. Available at: `https://oasis.caiso.com/mrioasis/logon.do`.
9. I. Podlubny, *Fractional differential equations: An introduction to fractional derivatives, fractional differential equations, to methods of their solution and some of their applications*, elsevier, 1998.

10. P. Warrier, P. Shah, Fractional order control of power electronic converters in industrial drives and renewable energy systems: a review, *IEEE Access*, **9** (2021), 58982–59009. https://doi.org/10.1109/ACCESS.2021.3073033
11. J. Zhao, H. Zhao, Y. Song, Z. Sun, D. Yu, Fast finite-time consensus protocol for high-order nonlinear multi-agent systems based on event-triggered communication scheme, *Appl. Math. Comput.*, **508** (2026), 129631. https://doi.org/10.1016/j.amc.2025.129631
12. H. Fu, Y. Kao, Robust sliding mode control of discrete fractional difference chaotic system, *Nonlinear Dyn.*, **113** (2025), 1419–1431. https://doi.org/10.1007/s11071-024-10279-6
13. Y. Kao, Y. Li, J. H. Park, X. Chen, Mittag-Leffler synchronization of delayed fractional memristor neural networks via adaptive control, *IEEE T. Neur. Net. Lear.*, **32** (2021), 2279–2284. https://doi.org/10.1109/TNNLS.2020.2995718
14. C. A. Monje, Y. Q. Chen, B. M. Vinagre, D. Xue, V. Feliu, *Fractional-order systems and controls: fundamentals and applications*, London: Springer, 2010.
15. A. Oustaloup, *La derivation non entiere: Theorie, synthese et applications*, Hermes science publications, 1995.
16. Y. Kao, C. Wang, H. Xia, Y. Cao, Projective synchronization for uncertain fractional reaction-diffusion systems via adaptive sliding mode control based on finite-time scheme, In: *Analysis and control for fractional-order systems*, Singapore: Springer, 2024. https://doi.org/10.1007/978-981-99-6054-5_8
17. V. I. Utkin, *Sliding modes in control and optimization*, Springer Science and Business Media, 2013.
18. Y. Yang, H. H. Zhang, Optimal model reference adaptive fractional-order proportional integral derivative control of idle speed system under varying disturbances, *Proc. I. Mech. Eng. Part I J. Sys.*, **239** (2025), 339–355. https://doi.org/10.1177/09596518241266670
19. M. A. Hossain, E. M. Gray, J. Lu, M. S. Alam, W. Hassan, M. Negnevitsky, Optimized model-free frequency control for renewable energy integration in islanded power systems, *IEEE T. Ind. Appl.*, **62** (2026), 2084–2096. https://doi.org/10.1109/TIA.2025.3603757
20. P. Li, R. Gao, C. Xu, Y. Li, A. Akgül, D. Baleanu, Dynamics exploration for a fractional-order delayed zooplankton-phytoplankton system, *Chaos Soliton. Fract.*, **166** (2023), 112975. https://doi.org/10.1016/j.chaos.2022.112975
21. Y. Zhao, Y. Sun, Z. Liu, Y. Wang, Solvability for boundary value problems of nonlinear fractional differential equations with mixed perturbations of the second type, *AIMS Math.*, **5** (2020), 557–567. https://doi.org/10.3934/math.2020037
22. H. Fu, Y. Kao, Synchronization of uncertain general fractional unified chaotic systems via finite-time adaptive sliding mode control, *Chaos*, **33** (2023), 043136. https://doi.org/10.1063/5.0130366
23. Y. Kao, Y. Cao, X. Chen, Global Mittag-Leffler synchronization of coupled delayed fractional reaction-diffusion Cohen-Grossberg neural networks via sliding mode control, *Chaos*, **32** (2022), 113123. https://doi.org/10.1063/5.0102787
24. K. Zhou, J. C. Doyle, *Essentials of robust control*, Upper Saddle River, NJ: Prentice hall, 1998.
25. Y. Li, Y. Chen, I. Podlubny, Mittag-Leffler stability of fractional order nonlinear dynamic systems, *Automatica*, **45** (2009), 1965–1969. https://doi.org/10.1016/j.automatica.2009.04.003

26. J. Wang, Y. Zhang, Ulam-Hyers-Mittag-Leffler stability of fractional-order delay differential equations, *Optimization*, **63** (2014), 1181–1190. https://doi.org/10.1080/02331934.2014.906597

27. A. A. Kilbas, H. M. Srivastava, J. J. Trujillo, *Theory and applications of fractional differential equations*, elsevier, 2006.

28. K. Diethelm, *The analysis of fractional differential equations*, Lecture notes in mathematics, 2010.

Appendix

Appendix A: Complete mathematical proofs

A.1. Preliminaries: Function spaces and integral inequalities

We recall the auxiliary inequalities used in the proofs. Throughout, $T > 0$ is fixed and $\alpha(\cdot) \in C^1[0,T]$ satisfies $0 < \alpha_{\min} \le \alpha(t) \le \alpha_{\max} < 1$ and $|\dot{\alpha}(t)| \le \rho$ on $[0,T]$.

Lemma 6.1. *(Young-type inequality in weighted spaces) Let $k : [0,T] \times [0,T] \to \mathbb{R}$ be measurable and let $w : [0,T] \to (0,\infty)$ be a weight. For $f \in L^2([0,T], w(\tau)\,d\tau)$, define*

$$(Kf)(t) = \int_0^t k(t,\tau)\, f(\tau)\, w(\tau)\, d\tau, \qquad t \in [0,T].$$

If $M > 0$ exists such that

$$\sup_{t\in[0,T]} \int_0^t |k(t,\tau)|\, w(\tau)\, d\tau \le M,$$

then $K : L^2([0,T], w\,d\tau) \to L^2([0,T], dt)$ is bounded and

$$\|Kf\|_{L^2[0,T]} \le M^{1/2}\, \|f\|_{L^2([0,T],w\,d\tau)}.$$

Proof. For each $t \in [0,T]$, the Cauchy–Schwarz inequality gives

$$|(Kf)(t)|^2 \le \Big(\int_0^t |k(t,\tau)|\, w(\tau)\, d\tau \Big)\Big(\int_0^t |k(t,\tau)|\, |f(\tau)|^2\, w(\tau)\, d\tau \Big).$$

Integrating over $t \in [0,T]$ and using the uniform bound by M yields

$$\int_0^T |(Kf)(t)|^2\, dt \le M \int_0^T \int_0^t |k(t,\tau)|\, |f(\tau)|^2\, w(\tau)\, d\tau\, dt.$$

By Fubini's theorem, we have

$$\int_0^T \int_0^t |k(t,\tau)|\, |f(\tau)|^2\, w(\tau)\, d\tau\, dt = \int_0^T |f(\tau)|^2\, w(\tau) \Big(\int_\tau^T |k(t,\tau)|\, dt \Big) d\tau.$$

Since $\int_\tau^T |k(t,\tau)|\, dt \le \sup_{t\in[0,T]} \int_0^t |k(t,s)|\, w(s)\, ds$ after the change in the variables $s = \tau$ and using the positivity of w, we obtain the desired estimate. (see, e.g., standard arguments in the weighted Young inequalities in fractional integral settings [27].) Taking the square roots completes the proof. □

Lemma 6.2. *(Uniform bounds for the fractional kernels) Define, the following for* $0 \le \tau < t \le T$*:*

$$k_C(t,\tau) = \frac{(t-\tau)^{-\alpha(t)}}{\Gamma(1-\alpha(t))}, \qquad k_H(t,\tau) = \frac{\left(\log\frac{t}{\tau}\right)^{-\alpha(t)}}{\Gamma(1-\alpha(t))} \quad (0 < \tau < t \le T).$$

Then the following uniform bounds hold:

(i)

$$\sup_{t\in[0,T]} \int_0^t |k_C(t,\tau)|\, d\tau \le \frac{T^{1-\alpha_{\min}}}{(1-\alpha_{\max})\,\Gamma(1-\alpha_{\max})} =: M_C;$$

(ii)

$$\sup_{t\in[0,T]} \int_0^t |k_H(t,\tau)|\, \frac{d\tau}{\tau} \le \frac{(\log T)^{1-\alpha_{\min}}}{(1-\alpha_{\max})\,\Gamma(1-\alpha_{\max})} =: M_H,$$

where $\log T > 0$ *(in the simulations and applications* $T > 1$*).*

Proof. (i) For a fixed $t \in (0,T]$, we have

$$\int_0^t (t-\tau)^{-\alpha(t)}\, d\tau = \frac{t^{1-\alpha(t)}}{1-\alpha(t)}.$$

Hence

$$\int_0^t |k_C(t,\tau)|\, d\tau = \frac{t^{1-\alpha(t)}}{(1-\alpha(t))\,\Gamma(1-\alpha(t))} \le \frac{T^{1-\alpha_{\min}}}{(1-\alpha_{\max})\,\Gamma(1-\alpha_{\max})},$$

using $t \le T$, $\alpha(t) \ge \alpha_{\min}$, and the monotonicity of $a \mapsto (1-a)^{-1}$ on $(0,1)$.

(ii) For a fixed $t \in (0,T]$ and $0 < \tau < t$, set $u = \log(t/\tau)$ so that $d\tau/\tau = -du$ and u runs from 0 to $\log t$. Then

$$\int_0^t \left(\log\frac{t}{\tau}\right)^{-\alpha(t)} \frac{d\tau}{\tau} = \int_0^{\log t} u^{-\alpha(t)}\, du = \frac{(\log t)^{1-\alpha(t)}}{1-\alpha(t)}.$$

Dividing by $\Gamma(1-\alpha(t))$ and using $\log t \le \log T$ (with $T > 1$) and the same bounds on $\alpha(t)$ completes the claim. □

A.2. Complete proof of Theorem 3.1 (well-posedness of the HCMF)

Recall the HCMF

$$\mathcal{M}^{\alpha(t)}[x](t) = \lambda\, C^{\alpha(t)}[x](t) + (1-\lambda)\,\mathcal{H}^{\alpha(t)}[x](t), \qquad \lambda \in [0,1],$$

where, for x in the space $\mathcal{X}$ of Definition 3.1, we have

$$C^{\alpha(t)}[x](t) = \int_0^t k_C(t,\tau)\, \dot{x}(\tau)\, d\tau, \qquad \mathcal{H}^{\alpha(t)}[x](t) = \int_0^t k_H(t,\tau)\, \frac{d}{d\tau}(\tau x(\tau))\, \frac{d\tau}{\tau}.$$

Part 1: Existence

Let $x \in \mathcal{X}$. By Definition 3.1, $x \in W^{1,2}[0,T]$, and hence its weak derivative $\dot{x} \in L^2[0,T]$. Define $g(\tau) = \tau x(\tau)$ for $\tau \in (0,T]$. Then $g'(\tau) = x(\tau) + \tau\dot{x}(\tau)$ in the weak sense. Moreover, since $x \in \mathcal{X}$, we have

$$\int_0^T |x(\tau)|^2 \frac{d\tau}{\tau} < \infty \quad \text{and} \quad \int_0^T |\tau\dot{x}(\tau)|^2 \frac{d\tau}{\tau} = \int_0^T \tau\,|\dot{x}(\tau)|^2\,d\tau \le T\|\dot{x}\|_{L^2}^2 < \infty.$$

Consequently,

$$\int_0^T |g'(\tau)|^2 \frac{d\tau}{\tau} \le 2\int_0^T |x(\tau)|^2 \frac{d\tau}{\tau} + 2\int_0^T |\tau\dot{x}(\tau)|^2 \frac{d\tau}{\tau} < \infty,$$

so $g' \in L^2([0,T], d\tau/\tau)$.

For the Caputo component, Lemma 6.2(i) yields $k_C(t,\cdot) \in L^1(0,t)$ uniformly in t. Since $\dot{x} \in L^2(0,T)$, the integral defining $C^{\alpha(t)}[x](t)$ is well-defined for almost everywhere (a.e.) $t \in [0,T]$.

For the Hadamard component, Lemma 6.2(ii) yields $k_H(t,\cdot) \in L^1((0,t), d\tau/\tau)$ uniformly in t, and $g' \in L^2((0,T), d\tau/\tau)$ implies that the integral defining $\mathcal{H}^{\alpha(t)}[x](t)$ is well-defined for a.e. $t \in [0,T]$.

Therefore, $\mathcal{M}^{\alpha(t)}[x](t)$ exists for a.e. $t \in [0,T]$, and hence defines an element of $L^2[0,T]$ as shown next.

Part 2: Boundedness in L^2

Step 2.1: Caputo component. Define $K_C : L^2[0,T] \to L^2[0,T]$ as

$$(K_C f)(t) = \int_0^t k_C(t,\tau)\,f(\tau)\,d\tau.$$

Using Lemma 6.1 with $w(\tau) \equiv 1$ and Lemma 6.2(i), we have

$$\|K_C f\|_{L^2[0,T]} \le M_C^{1/2}\,\|f\|_{L^2[0,T]}.$$

Applying this with $f = \dot{x}$ gives

$$\|C^{\alpha(t)}[x]\|_{L^2[0,T]} \le M_C^{1/2}\,\|\dot{x}\|_{L^2[0,T]} \le M_C^{1/2}\,\|x\|_{W^{1,2}[0,T]}. \tag{6.1}$$

Step 2.2: Hadamard component. Define $K_H : L^2([0,T], d\tau/\tau) \to L^2[0,T]$ as

$$(K_H f)(t) = \int_0^t k_H(t,\tau)\,f(\tau)\,\frac{d\tau}{\tau}.$$

Applying Lemma 6.1 with the weight $w(\tau) = 1/\tau$ and using Lemma 6.2 (ii), we have

$$\|K_H f\|_{L^2[0,T]} \le M_H^{1/2}\,\|f\|_{L^2([0,T],d\tau/\tau)}.$$

Taking $f = g'$ yields

$$\|\mathcal{H}^{\alpha(t)}[x]\|_{L^2[0,T]} \le M_H^{1/2}\,\|g'\|_{L^2([0,T],d\tau/\tau)} \le M_H^{1/2}\,(\|x\|_{L^2(d\tau/\tau)} + \|\tau\dot{x}\|_{L^2(d\tau/\tau)}). \tag{6.2}$$

Since $\|\tau\dot{x}\|_{L^2(d\tau/\tau)}^2 = \int_0^T \tau|\dot{x}(\tau)|^2\,d\tau \le T\|\dot{x}\|_{L^2}^2$, we obtain

$$\|g'\|_{L^2(d\tau/\tau)} \le \|x\|_{L^2(d\tau/\tau)} + \sqrt{T}\,\|\dot{x}\|_{L^2} \le (1 + \sqrt{T})\,\|x\|_{\mathcal{X}},$$

and hence

$$\|\mathcal{H}^{\alpha(t)}[x]\|_{L^2[0,T]} \leq M_H^{1/2}(1 + \sqrt{T})\,\|x\|_{\mathcal{X}}. \tag{6.3}$$

Step 2.3: Hybrid functional. Combining (6.1) and (6.3) and using $\|x\|_{W^{1,2}} \leq \|x\|_{\mathcal{X}}$ gives

$$\|\mathcal{M}^{\alpha(t)}[x]\|_{L^2[0,T]} \leq \lambda\,\|C^{\alpha(t)}[x]\|_{L^2} + (1-\lambda)\,\|\mathcal{H}^{\alpha(t)}[x]\|_{L^2} \leq C\,\|x\|_{\mathcal{X}},$$

where one may take, for instance, the following:

$$C := \lambda\,M_C^{1/2} + (1-\lambda)\,M_H^{1/2}(1 + \sqrt{T}).$$

Thus $\mathcal{M}^{\alpha(t)} : \mathcal{X} \to L^2[0,T]$ is bounded.

Part 3: Linearity

Let $a, b \in \mathbb{R}$ and $x_1, x_2 \in \mathcal{X}$. The linearity of integration yields the linearity of both $C^{\alpha(t)}$ and $\mathcal{H}^{\alpha(t)}$, and hence

$$\begin{aligned}\mathcal{M}^{\alpha(t)}[ax_1 + bx_2](t) &= \lambda\,C^{\alpha(t)}[ax_1 + bx_2](t) + (1-\lambda)\,\mathcal{H}^{\alpha(t)}[ax_1 + bx_2](t)\\ &= a(\lambda\,C^{\alpha(t)}[x_1](t) + (1-\lambda)\,\mathcal{H}^{\alpha(t)}[x_1](t)) + b(\lambda\,C^{\alpha(t)}[x_2](t) + (1-\lambda)\,\mathcal{H}^{\alpha(t)}[x_2](t))\\ &= a\,\mathcal{M}^{\alpha(t)}[x_1](t) + b\,\mathcal{M}^{\alpha(t)}[x_2](t).\end{aligned}$$

This completes the proof of Theorem 3.1.

A.3. Empirical justification of the hybrid weight $\lambda = 0.7$

This subsection provides an empirical justification for the representative choice $\lambda = 0.7$ adopted in the numerical studies. We emphasize that λ is not claimed to be theoretically optimal; instead, it is selected as a practically meaningful balance parameter reflecting the typical operating conditions of modern power grids.

The justification is based on a statistical analysis of wide-area frequency measurements and load-generation data from US power systems, including the FNET/GridEye, PJM, and CAISO datasets over the period 2020–2023.

Fast time-scale activity. Let $\mathrm{RoCoF}_i(t)$ denote the RoCoF signals associated with the i-th disturbance event. We define the average fast time-scale energy as

$$E_f = \frac{1}{N}\sum_{i=1}^{N}\int_0^T |\mathrm{RoCoF}_i(t)|^2\,dt,$$

which quantifies the intensity of rapid frequency excursions driven by inverter-based and converter-dominated dynamics.

Slow time-scale variability. For the normalized load and renewable generation profiles $L_j(t)$, we define the slow variation index

$$V_s = \frac{1}{M}\sum_{j=1}^{M}\int_0^T \left|\frac{d}{dt}\log(1 + L_j(t))\right|^2\,dt,$$

which captures the long-memory effects associated with gradual load evolution and renewables' intermittency.

Relative time-scale contribution. To assess the relative importance of fast and slow dynamics, we consider the dimensionless ratio

$$r = \frac{E_f}{E_f + V_s}.$$

Across 127 representative disturbance events, the empirical distribution of r yields

$$r = 0.69 \pm 0.08 \quad \text{(mean} \pm \text{standard deviation).}$$

This result indicates that, under mixed operating conditions, the fast and slow dynamic components contribute comparably to the overall system response. Accordingly, selecting a hybrid weight $\lambda \approx 0.7$ provides a balanced emphasis between the Caputo-type short-memory contribution and the Hadamard-type long-memory contribution.

We stress that this choice is representative rather than optimal, and is adopted to ensure consistency and clarity in the numerical validation. The sensitivity of the control performance with respect to λ is further examined in Section 6, confirming that the proposed framework remains robust over a broad range of hybrid weights.

Appendix B: Proof of Theorem 4.1 and Corollary 4.2

B.1. Proof of Theorem 4.1 (Mittag-Leffler stability)

We provide a complete proof of Theorem 4.1, establishing Mittag-Leffler stability for the closed-loop system under bounded order variation.

B.1.1. Preliminaries and notation

Recall the closed-loop system

$$\mathcal{M}^{\alpha(t)}[\mathbf{x}](t) = \mathbf{A}_{\text{cl}}\mathbf{x}(t) + \mathbf{F}\mathbf{d}(t), \tag{6.4}$$

with $\mathbf{A}_{\text{cl}} = \mathbf{A} - \mathbf{B}\mathbf{K}$. Throughout this proof, we write

$$\lambda_P^{\min} = \lambda_{\min}(\mathbf{P}), \quad \lambda_P^{\max} = \lambda_{\max}(\mathbf{P}), \quad \lambda_Q^{\min} = \lambda_{\min}(\mathbf{Q}),$$

where $\mathbf{P}, \mathbf{Q} \succ 0$ are the matrices appearing in the LMI (4.2).

The fractional order $\alpha(t)$ satisfies Assumption 4.1, i.e.,

$$0 < \alpha_{\min} \le \alpha(t) \le \alpha_{\max} < 1, \qquad |\dot{\alpha}(t)| \le \rho.$$

The disturbance is bounded by $\|\mathbf{d}(t)\| \le d_{\max}$.

B.1.2. Construction of the extended Lyapunov functional

Define the extended Lyapunov functional

$$V(t, \mathbf{x}, \alpha) = \mathbf{x}^\top \mathbf{P}\mathbf{x} \; + \; \eta \int_0^t e^{-\delta(t-s)} (\alpha(s) - \alpha_0)^2 \, ds, \tag{6.5}$$

where $\alpha_0 = (\alpha_{\min} + \alpha_{\max})/2$ and $\eta, \delta > 0$ are positive parameters to be chosen later. The second term penalizes deviations of the fractional order from its nominal value, thereby capturing the effect of order variations.

B.1.3. Action of the hybrid memory functional on V

Applying the hybrid memory functional $\mathcal{M}^{\alpha(t)}$ to V and using the linearity established in Theorem 3.1 yields

$$\begin{aligned}\mathcal{M}^{\alpha(t)}[V](t) &= \mathcal{M}^{\alpha(t)}[\mathbf{x}^{\top}\mathbf{P}\mathbf{x}](t) + \eta\,\mathcal{M}^{\alpha(t)}\left[\int_0^t e^{-\delta(t-\cdot)}(\alpha-\alpha_0)^2\,ds\right](t)\\ &=: V_1(t) + \eta V_2(t).\end{aligned} \tag{6.6}$$

For the first term, using the bilinearity of the quadratic form and the linearity of the HCMF, we obtain

$$\begin{aligned}V_1(t) &= 2\mathbf{x}^{\top}\mathbf{P}\,\mathcal{M}^{\alpha(t)}[\mathbf{x}](t) + R_1(t)\\ &= 2\mathbf{x}^{\top}\mathbf{P}(\mathbf{A}_{\mathrm{cl}}\mathbf{x} + \mathbf{F}\mathbf{d}) + R_1(t),\end{aligned} \tag{6.7}$$

where the remainder $R_1(t)$ satisfies the estimate

$$|R_1(t)| \leq c_1\rho\,\|\mathbf{x}(t)\|^2$$

with a uniform constant c_1 depending only on $\lambda_P^{\max}$, $\alpha_{\min}$, $\alpha_{\max}$, and the kernel bounds established in Lemma A.1 (Appendix A). This estimate relies on the boundedness of $\dot{\alpha}(t)$ and the uniform bounds for the kernels of $C^{\alpha(t)}$ and $\mathcal{H}^{\alpha(t)}$.

For the second term, a direct computation using the definition of the HCMF together with the boundedness of $\dot{\alpha}(t)$ leads to

$$V_2(t) \leq -\delta\int_0^t e^{-\delta(t-s)}(\alpha(s)-\alpha_0)^2 ds + c_2\rho\,\|\mathbf{x}(t)\|^2,$$

where $c_2 > 0$ again depends only on the kernel bounds.

Combining (6.6), (6.7), and the estimate for V_2, we obtain

$$\mathcal{M}^{\alpha(t)}[V](t) \leq \mathbf{x}^{\top}(\mathbf{A}_{\mathrm{cl}}^{\top}\mathbf{P} + \mathbf{P}\mathbf{A}_{\mathrm{cl}})\mathbf{x} + 2\mathbf{x}^{\top}\mathbf{P}\mathbf{F}\mathbf{d} + (c_1+\eta c_2)\rho\|\mathbf{x}\|^2 - \eta\delta\int_0^t e^{-\delta(t-s)}(\alpha(s)-\alpha_0)^2 ds. \tag{6.8}$$

B.1.4. Using the LMI condition

The LMI (4.2) implies, by the Schur complement, that for any vector $\mathbf{z} \in \mathbb{R}^n$ and any scalar w, we have

$$\mathbf{z}^{\top}(\mathbf{A}_{\mathrm{cl}}^{\top}\mathbf{P} + \mathbf{P}\mathbf{A}_{\mathrm{cl}} + \mathbf{Q})\mathbf{z} + 2\mathbf{z}^{\top}\mathbf{P}\mathbf{F}w + \rho\mathbf{z}^{\top}\mathbf{P}\mathbf{z} \leq \gamma w^2 + \gamma\rho^2\|\mathbf{z}\|^2.$$

Applying this inequality with $\mathbf{z} = \mathbf{x}(t)$ and $w = \|\mathbf{d}(t)\|$ (noting that $|\mathbf{d}^{\top}\mathbf{F}^{\top}\mathbf{P}\mathbf{x}| \leq \|\mathbf{P}\mathbf{F}\|\,\|\mathbf{x}\|\,\|\mathbf{d}\|$) yields

$$\mathbf{x}^{\top}(\mathbf{A}_{\mathrm{cl}}^{\top}\mathbf{P} + \mathbf{P}\mathbf{A}_{\mathrm{cl}})\mathbf{x} + 2\mathbf{x}^{\top}\mathbf{P}\mathbf{F}\mathbf{d} \leq -\mathbf{x}^{\top}\mathbf{Q}\mathbf{x} + \gamma d_{\max}^2 + (\gamma\rho^2 - \rho)\|\mathbf{x}\|^2.$$

Insert this bound into (6.8) and choose $\eta = c_1/(2c_2)$. Then the terms containing $\rho\|\mathbf{x}\|^2$ combine to give a coefficient

$$\gamma\rho^2 - \rho + (c_1+\eta c_2)\rho = \gamma\rho^2 - \frac{\rho}{2} \leq -\frac{\rho}{4},$$

provided that ρ is small enough that $\gamma\rho^2 \leq \rho/4$. This condition is compatible with the empirical bound on ρ reported in Remark 4.1, where $\rho \leq 0.03\,\mathrm{s}^{-1}$. Consequently, we have

$$\mathcal{M}^{\alpha(t)}[V](t) \leq -\lambda_Q^{\min}\|\mathbf{x}\|^2 + \gamma d_{\max}^2 - \frac{\rho}{4}\|\mathbf{x}\|^2 - \eta\delta\int_0^t e^{-\delta(t-s)}(\alpha(s)-\alpha_0)^2 ds. \tag{6.9}$$

B.1.5. Applying the variable-order comparison lemma

Inequality (6.9) can be written as

$$\mathcal{M}^{\alpha(t)}[V](t) \leq -\mu V(t) + \gamma d_{\max}^2,$$

where

$$\mu = \min\left\{\frac{\lambda_Q^{\min} + \rho/4}{\lambda_P^{\max}}, \delta\right\}.$$

The variable-order fractional comparison lemma (see Lemma B.1 below) then guarantees the existence of the constants $M_0, \beta > 0$, depending on μ and $\alpha_{\min}$, such that

$$V(t) \leq M_0 E_{\alpha_{\min}}(-\beta t^{\alpha_{\min}}) V(0) + \frac{\gamma d_{\max}^2}{\mu}.$$

Since $V(t) \geq \lambda_P^{\min} \|\mathbf{x}(t)\|^2$ and $V(0) \leq \lambda_P^{\max} \|\mathbf{x}(0)\|^2 + \eta(\alpha_{\max} - \alpha_{\min})^2/\delta$, we finally obtain

$$\|\mathbf{x}(t)\| \leq M\, E_{\alpha_{\min}}(-\beta t^{\alpha_{\min}}) \|\mathbf{x}(0)\| + \frac{d_{\max}}{\sigma},$$

with

$$M = \sqrt{\frac{\lambda_P^{\max} M_0}{\lambda_P^{\min}}}, \qquad \sigma = \sqrt{\frac{\mu \lambda_P^{\min}}{\gamma}}.$$

This completes the proof of Theorem 4.1.

B.1.6. Auxiliary lemma

Lemma 6.3. *(Variable-order fractional comparison lemma) Let* $v(t) \geq 0$ *satisfy*

$$\mathcal{M}^{\alpha(t)}[v](t) \leq -\mu v(t) + \nu, \qquad t \geq 0,$$

with $\mu > 0$, $\nu \geq 0$, *and* $\alpha(t)$ *satisfying Assumption 4.1. Then the constants* $M_0, \beta > 0$, *exist depending only on* μ, $\alpha_{\min}$, *and* $\alpha_{\max}$, *such that*

$$v(t) \leq M_0 E_{\alpha_{\min}}(-\beta t^{\alpha_{\min}}) v(0) + \frac{\nu}{\mu}.$$

Proof. The proof follows by constructing a suitable majorant fixed-order problem with order $\alpha_{\min}$ and applying the classical Mittag-Leffler stability estimates for constant-order fractional differential inequalities [25]. The dependence on $\alpha_{\max}$ enters through the uniform bounds on the kernels of $\mathcal{M}^{\alpha(t)}$. □

B.2. Proof of Corollary 4.2 (discretization robustness)

Corollary 4.2 follows directly from Theorem 4.2 (Ulam-Hyers stability) once the local truncation error of the discretization scheme is quantified. Let $\mathbf{x}_h(t)$ be the numerical solution obtained with a

Grünwald-Letnikov discretization of step size h. Standard error analysis for the fractional operators [28] yields a local truncation error bound

$$\|\tau_h(t)\| \le Lh^p,$$

where p is the order of the method ($p = 1$ for the basic Grünwald-Letnikov scheme) and L depends on the bounds for derivatives of the state and the kernel functions.

The discrete solution satisfies a perturbed continuous equation

$$\mathcal{M}^{\alpha(t)}[\mathbf{x}_h](t) = \mathbf{A}_{\mathrm{cl}}\mathbf{x}_h(t) + \mathbf{F}\mathbf{d}(t) + \tau_h(t),$$

with $\|\tau_h(t)\| \le Lh^p$. Taking $\varepsilon = Lh^p$ in Theorem 4.2 gives

$$\|\mathbf{x}_h(t) - \mathbf{x}(t)\| \le CLh^p,$$

where C is the Ulam-Hyers constant from Theorem 4.2. Setting $C_d = CL$ and choosing h_0 to be small enough that the truncation error remains within the validity range of the theorem yields the desired uniform bound. This completes the proof of Corollary 4.2.